Research Square

Preprints are preliminary reports that have not undergone peer review.
They should not be considered conclusive, used to inform clinical practice,
or referenced by the media as validated information.

Long-range Ret retrograde signaling drives subtype fate and functional identity in a sensory circuit

Alex Nechiporuk

nechipor@ohsu.edu

Oregon Health and Science Univ https://orcid.org/0000-0002-8295-8188

Jacqueline McVay

Oregon Health and Science Univ https://orcid.org/0000-0002-6358-2840

Lauren Miller

Oregon Health and Science Univ

Katherine Pinter

National Institute of Child Health and Human Development

Riley Buese1

Oregon Health and Science Univ

Ryan Doan

Oregon Health & Science University https://orcid.org/0000-0002-6944-3921

Kelly Monk

Oregon Health & Science University https://orcid.org/0000-0003-1803-3495

Katie Kindt

National Institute on Deafness and Other Communication Disorders https://orcid.org/0000-0002-1065-8215

Article

Keywords:

Posted Date: August 22nd, 2026

DOI: https://doi.org/10.21203/rs.3.rs-10732516/v1

License: This work is licensed under a Creative Commons Attribution 4.0 International License.
Read Full License

Additional Declarations: There is **NO** Competing Interest.

Long-range Ret retrograde signaling drives subtype fate and functional identity in a sensory circuit

Jacqueline R McVay[1,2,5], Lauren N Miller[1,5], Katherine Pinter[3], Riley A Buese[1], Ryan A Doan[4], Kelly R Monk[4], Katie S Kindt[3], and Alex V Nechiporuk[1*]

[1] Department of Cell, Developmental & Cancer Biology, Oregon Health & Science University, Portland, Oregon, USA.
[2] Neuroscience Graduate Program, The Vollum Institute, Oregon Health & Science University, Portland, Oregon, USA.
[3] Section on Sensory Cell Development and Function, National Institute on Deafness and Other Communication Disorders, National Institutes of Health, Bethesda, USA.
[4] The Vollum Institute, Oregon Health & Science University, Portland, Oregon, USA.
[5] co-first authors
* Correspondence to nechipor@ohsu.edu

Abstract

During development, neurons extend axons to appropriate targets and acquire distinct molecular and functional identities. Neurotrophins use retrograde signaling to regulate axon targeting and neuronal survival, yet whether this signaling also instructs functional neuronal subtype maturation remains poorly understood. Using the mechanosensory circuit of the zebrafish posterior lateral line (pLL), we investigate two transient neuronal subtypes, pioneers and followers. Their progenitors initially adopt a follower-like state, with a subset transitioning to pioneers that express high levels of the Gdnf receptor Ret. Pioneers project axons early and preferentially innervate distal targets with distinct postsynaptic physiological properties, whereas low-Ret followers project later to proximal targets. We find that pioneer-derived terminals are significantly less responsive to sensory stimulation than follower-derived terminals, revealing functional specialization between these neuronal subtypes. We show that long-range Ret signaling is required to stabilize pioneer identity and establish subtype-specific physiological properties. Loss of Ret drives transcriptional reversion toward the follower program and convergence of postsynaptic physiology. These findings identify retrograde Ret signaling as a mechanism that couples target-derived cues to neuronal identity and functional circuit diversification.

Methods

Animal husbandry

All experiments were approved by the Institutional Animal Care and Use Committee at Oregon Health & Science University (Protocol#TR03_IP00000495). Adult zebrafish were maintained at 28.5 °C. Embryos were derived from natural matings and raised in embryo medium either at 28.5 °C (standard) or at 22°C and 25°C (to slow development). Embryo staging was conducted according to Kimmel *et al.*[1] Strains utilized in this study were *AB, Tubingen, TgBAC(*neurod1:EGFP*)^{nl1} [2], *ret*^{hu2846} [3], Tg*(−8.0cldnB:LY-EGFP)*^{zf106} [4], Tg(*rpz5:mRuby*)^{nl27} [5], Tg(*prim:lyn2-mCherry*)[6], Tg*(myo6b:GCaMP6s-CAAX)*^{idc1} [7], and Tg(*en.sill,hsp70l:GCaMP6s*)^{idc8} [7].

Embryo dissociation

TgBAC(*neurod1:EGFP*)^{nl1} wildtypes and *ret* mutants (identified by severe axon truncation at 48 hours post-fertilization (hpf)) were dissociated following a modified version of the protocol from the Lawson lab[8]. Briefly, 1.2 mL of protease solution (0.25% trypsin, 1mM EDTA, pH 8.0 in PBS) was warmed in a 24-well plate at 28.5°C for 10 min. Embryos were then transferred to a 1.5 mL tube and embryo media was removed and replaced with 100 µL of calcium-free Ringer's solution. Embryos were deyolked by gentle pipetting 15 times with a p200, then transferred to the warmed protease solution. 27 µL of Collagenase P/HBSS (160 U/mL) was added followed by pipette mixing. Plates were incubated at 28.5 °C for 15 min with trituration every 5 min by pipetting with a p1000. Digestion was halted by addition of 6x stop solution (30% calf serum, 6mM $CaCl_2$, PBS), and the entire volume of each well was transferred to a microcentrifuge tube. Tubes were spun at 350 x g at 4°C for 5 min and supernatant was removed. The cell pellet was rinsed by adding 1 mL chilled suspension solution (1% FBS, 0.8mM $CaCl_2$, 50 U/mL penicillin, 0.05mg/mL streptomycin, DMEM) and then spun down again at 350 x g at 4°C for 5 min; the by supernatant was removed. The cell pellet was resuspended in 700 µL suspension solution and passed through a 70 µm cell strainer into a FACs tube on ice.

FACS

Dissociated cells were sorted based on EGFP fluorescence and gated such that only the top 2% brightest EGFP+ cells were collected for analysis at 48 hpf. Cells were sorted into 50 µL 1x PBS/2% BSA in siliconized microcentrifuge tubes. Cell suspension was spun down at 350 x g at 4°C for 5 min and the top 50 µL was removed to enrich for viable cells.

Single cell RNA sequencing

EGFP+ cells from 50–100 dissociated embryos were used to create scRNA-seq libraries with Single Cell 3′ v3 (10X Genomics) gene expression kits following manufacturer protocol. Samples were sequenced targeting ~50,000 reads per cell. Reads were aligned to GRCz11 using CellRanger version 3.1.0 (10X Genomics). Primary analysis was performed using Seurat v4[9]. Data were filtered to retain cells with 1,000-7,500 UMI counts and <5% mitochondrial RNA. After quality control filtering, 7,216 wild-type and 8,011 mutant cells were retained[10]. Data sets can be publicly accessed at The National Center for Biotechnology and Information (NCBI) through the Gene Expression Omnibus: GSE264323 and GSE342313. Individual cluster identities were determined by comparing 5-10 top differentially expressed markers to published scRNA-seq data sets and the marker expression data base at 48 hpf[11–16]. The pLL cluster was identified by expression of known lateral line markers but lack of marker expression of other cranial sensory neurons (*irx1a* and *phox2bb*) as well as anterior lateral line neurons (*alcama*). This cluster was then subjected to unsupervised subclustering, which yielded two distinct subpopulations, pioneers and followers.

Fluorescent in situ hybridization (RNAscope®)

Embryos were fixed in BT-fix (4% paraformaldehyde, 0.15 mM $CaCl_2$, 4% sucrose, 0.1M PO_4 buffer, pH = 7.3) overnight at 4°C. Fixative was removed by 3 × 5 min washes in 1x PBS/0.01% Tween, followed by dehydration in a methanol series. Samples were then stored at −20 °C until processing. The RNAscope® Multiplex Fluorescent Detection Kit v2 following the Gross-Thebing *et al.* 2014 protocol[17] was used with several modifications. Methanol was removed and samples were rehydrated with 1x PBS − 0.01% Tween. The protease step was omitted for all samples. Samples were then incubated overnight at 40 °C in 1:50 diluted probes. Probes were recovered and samples were washed in 0.2X SSCT (0.2X SSC and 0.01% Tween). Samples were then incubated at 40 °C according to the protocol in Amp1-3 using 2 drops of solution. After amplification, 2 drops of HRP matching the probe channel were added and samples were again incubated at 40°C. Opal dyes 405, 570, and 650 were used at 1:1000. Washes between Amp solutions, HRP solutions, and Opal dyes were conducted using 1 quick rinse and 2 × 15min 0.2x SSCT rinses. HRP blocker was used between channels prior to conjugating new HRPs but omitted before antibody incubation.

Immunofluorescence

Fluorescent *in situ* hybridization was followed by immunostaining to enhance transgene fluorescence. Samples underwent post fixation in 4% PFA for 10 min at RT. Fixative was then removed and embryos were washed in PBST (1x PBS/0.1% Triton) 3 × 20 min and blocked with 2% goat serum for 1 h at room temperature. Primary antibody, anti-GFP (Aves Labs GFP-1020) 1:1000, was added and samples were incubated overnight at 4°C with agitation. The primary antibody was

removed with 3 × 15min washes with PBST and secondary antibody, goat anti-chick (Invitrogen A11039) 1:1000, was added and incubated for 4h at 4°C with agitation. Secondary antibody was washed out the same way.

To label ribbon synapses, larvae at 5 days post-fertilization (dpf) were fixed with 4% PFA in PBS for 3-4 h at 4°C. After fixation, samples were washed 5 × 5 min in 1x PBS + 1% DMSO, 0.5% Triton X-100, 0.1% Tween-20 (PBDTT). Larvae were then blocked overnight at 4 °C in blocking solution (2% goat serum, 1% bovine serum albumin, 2% fish skin gelatin in PBDTT). After block, larvae were incubated in primary antibodies: Rabbit anti-MYO7A (Proteus 25-6790) 1:1000, mouse anti-pan-MAGUK (Millipore MABN7) 1:500, and mouse anti-pan-CTPB (Santacruz SC-55502) 1:1000, in antibody solution (1% BSA in PBDTT) overnight, nutating at 4°C. The next day, the larvae were washed 5 × 5 min in PBDTT to remove the primary antibodies. Secondary antibodies were added at 1:1000 in antibody solution (goat anti-rabbit Alexa 488 nm, goat anti-mouse IgG2a Alexa 568 nm, goat anti-mouse IgG1 Alexa 647 nm (ThermoFisher A11008, A21134, and A21240), and larvae were incubated for 2 h at room temperature. Secondary antibodies were removed by washing 4 × 5 min in PBDTT. Larvae were mounted on glass slides with Prolong Gold (ThermoFisher) using No. 1.5 coverslips.

Confocal microscopy

For live imaging, embryos were mounted in 1.5% low melting point agarose in embryo medium[18] on a glass cover slip and submersed in embryo media containing 0.02% tricaine (tricaine methanesulfonate, Syndel, MS-222). To observe axon extension, embryos were imaged at 24 and 72 hpf timepoints, with 24 hpf samples being removed from the agarose and placed at 28.5°C until 72 hpf imaging. All live imaging was performed on an upright Fluoview3000 confocal microscope (Olympus) using a 40x/1.25 NA silicon oil immersion lens. Images through the pLLg or axon terminals were acquired with sufficient depth to capture the entire structure and all labeled cells/growth cones present. For fixed imaging of RNAscope®, embryos were mounted in 50% glycerol/1x PBS and imaged on an upright Fluoview3000 confocal microscope (Olympus) using a 40x/1.4 NA oil immersion lens.

Fixed samples of ribbon synapses were imaged on an upright Zeiss LSM 980 laser-scanning confocal microscope with an Airyscan 2 attachment using Zen (Carl Zeiss) and a 63x/1.4 NA Plan Apo oil immersion objective lens. Airyscan z-stacks were acquired every 0.15 µm with a 0.043 µm xy pixel size. The Airyscan z-stacks were autoprocessed in 3D.

Quantification of axon targeting

To mosaically label neurons, embryos derived from *ret*^{hu2846}/+;TgBAC(*neurod1:EGFP*)^{nl1} incrosses were injected with 5 picograms of *pDestTol2-hsp70-mCherry-SILL* plasmid[5]. To track axon pLL targeting, embryos were first imaged at 24 hpf. Animals containing 1 or 2 mCherry-positive pLL pioneers - axon terminals embedded within the pLLP - were saved and re-imaged at 72 hpf. At that stage, NM targets were recorded. *ret*^{hu2846} embryos were identified by genotyping after imaging[19].

Quantification of fluorescent *in situ* hybridization

Confocal stacks of the pLLg were exported to Imaris (Bitplane) and analyzed using the Cells function. The volume encompassing pLL neuron cell bodies were outlined using the green channel from TgBAC(*neurod1:EGFP*)^{nl1}. The amplification from RNAscope® results in detectable individual mRNA transcripts, so fluorescent puncta were totaled in each cell.

Quantification of ribbon synapses

To identify and quantify synaptic puncta (presynaptic ribbons and postsynapses), an automated synapse quantification method using a customized Fiji-based macro, 'Complete Synapse Counter v5.2' (https://github.com/KindtLab/CompleteSynpaseCounter5.2) was used as previously described[20]. Before using this macro, each channel was background subtracted using rolling-ball radius correction and then max-intensity projected in z. A mask was generated by manually outlining the region containing the hair cells in the reference channel (Myo7a). This mask was then applied to the *z*-projection of each synaptic component. Each masked image was then analyzed using the customized Fiji-based macro. For the puncta analysis, the following minimum size thresholds were applied: CTBP 0.025 μm^2 and MAGUK 0.04 μm^2, along with a circularity factor between 0.1 and 0.5. ROIs of puncta were then applied to the original *z*-projection to get the average intensity and area of each punctum. To recognize paired synaptic components, pre- and postsynaptic ROIs with positive overlap within 2 pixels were counted as paired components[20].

Transmission electron microscopy

Zebrafish were anesthetized using tricaine and examined under a fluorescence microscope to visualize and transect 2-3 body segments anterior to L5. Samples were then immersed in a modified Karnovsky's fixative consisting of 2% glutaraldehyde and 4% paraformaldehyde in 0.1 M sodium cacodylate buffer (pH 7.4). Microwave-assisted fixation was performed in a PELCO BioWave processor (Ted Pella) using the following cycle: 100 W for 1 min, off for 1 min, 100 W for 1 min, off for 1 min, 450 W for 20 s, and off for 20 s. This cycle was repeated five times, after which the samples were allowed to continue fixing overnight at 4°C. The next day, samples were rinsed three times for

10 min each in 0.1 M sodium cacodylate buffer at room temperature. A secondary fixative of 2% osmium tetroxide was freshly prepared by mixing 2 ml of 0.2 M sodium cacodylate + 0.2 M imidazole solution (pH 7.5) with 2 ml of 4% osmium tetroxide. This solution was added to the samples, followed by microwave processing using the cycle: 100 W for 1 min, off for 1 min, 100 W for 1 min, off for 1 min, 450 W for 20 s, and off for 20 s, repeated five times. Samples were then incubated for an additional 2 h at room temperature. After removal of the osmium tetroxide, samples were washed three times in deionized water (10 min per wash). UranyLess (Electron Microscopy Sciences) was added to the samples, and microwave processing was carried out: 450 W for 1 min, off for 1 min, and 450 W for 1 min. Samples remained in UranyLess overnight at 4°C. The following day, UranyLess was removed, and samples were washed three times with deionized water (10 min each). A graded ethanol series (25:75, 50:50, 70:30, 80:20, 95:5, and 100:0 ethanol:water) was prepared. Samples were dehydrated through this series (25%, 50%, 70%, 80%, and 95% ethanol), with each step involving microwave treatment at 250 W for 45 s followed by a 10 min incubation at room temperature. Samples were then transferred to 100% ethanol and microwaved: 250 W for 1 min, off for 1 min, and 250 W for 1 min, followed by 10 min at room temperature. This 100% ethanol step was repeated two additional times (total of three changes). Dehydration continued with three changes of 100% EM-grade acetone, each involving microwave processing at 250 W for 1 min, off for 1 min, and 250 W for 1 min, followed by a 10 min incubation at room temperature. A 1:1 mixture of Araldite 812 and 100% acetone was then added, and samples were allowed to infiltrate overnight at room temperature. The following day, fresh Araldite 812 resin was prepared. Using a stereomicroscope (Zeiss Stemi 508), samples were carefully oriented in molds for optimal sectioning alignment. After 4–6 h at room temperature, the blocks were transferred to a 65 °C oven for polymerization for at least 48 h. For all samples, semithin sections (400 nm thick) were cut and stained with toluidine blue, then examined under a light microscope (Leica DM 300) to assess quality prior to ultrathin sectioning. Ultrathin sections (60 nm) were cut and collected onto 100-mesh Formvar-coated grids (#FCF100-Cu; EMS). Sections were counterstained with UranyLess (Electron Microscopy Sciences) and 3% lead citrate (Electron Microscopy Sciences). Images were acquired using an FEI Tecnai T12 transmission electron microscope equipped with an Advanced Microscopy Techniques CCD camera.

Fluid jet stimulation and Imaging of GCaMP6s in neuromast hair cells and afferent terminals

For functional imaging, 4-6 dpf larvae were anesthetized in 0.04% Tricaine-S (tricaine methanesulfonate, Western Chemical, TRS1) and pinned to a Sylgard-filled perfusion chamber at the head and tail. Several small pins were used to secure the tail, rather than piercing the notochord near the tail to avoid damaging the terminal neuromasts. After pinning, larvae were paralyzed by

injection of 125 μM α-bungarotoxin (Tocris, 2133) into the heart cavity, as previously described[21]. Larvae were then rinsed with E3 embryo media to remove the tricaine. Larvae were then immersed in extracellular imaging solution (in mM: 140 NaCl, 2 KCl, 2 $CaCl_2$, 1 $MgCl_2$ and 10 HEPES, pH 7.3, OSM 310±10). To stimulate lateral line hair cells, a fluid jet comprised of a pressure clamp (HSPC-1, ALA Scientific) and glass pipette was used. The glass pipette was pulled and broken to an inner diameter 40-50 μm and filled with extracellular imaging solution. A 2-s or 500-ms pulse of positive or negative pressure was used to deflect neuromast hair cells along the anterior-posterior axis of the fish. Stimuli were titrated to deflect hair cell kinocilia 5-10 μm.

Calcium responses in hair cells or the afferent process were acquired on a Swept-field confocal system built on a Nikon FN1 upright microscope (Bruker) with a 60×/1.0 NA CFI Fluor water-immersion objective. The microscope was equipped with a Rolera EM-C2 EMCCD camera (QImaging), controlled using Prairie view 5.4 (Bruker). GCaMP6 s was excited using a 488 nm solid state laser and used a dual band-pass 488/561 nm filter set (59904-ET, Chroma). Each neuromast (proximal neuromasts L1 or L2, and distal neuromasts L5 or termNM1-3) was stimulated twice with an inter-stimulus interval of ∼2 min. Five *z*-slices in the presynaptic plane of the hair cells (1.0 μm step) or five z-slices containing the postsynaptic afferent terminal (1.5 μm step) were collected per timepoint for 80 timepoints at a frame rate of 20 ms for a total of ∼100 ms per *z*-stack and a total acquisition time of ∼8 s.

Acquired images were converted into TIFF series for processing. *Z*-stacks were average projected, registered and spatially smoothed using a Gaussian filter (size=3, sigma=2) as described previously[7]. The first ten timepoints (∼1 s) were removed to reduce the effect of initial photobleaching. Registered average projections were analyzed in Fiji for intensity measurements. The Time Series Analyzer V3 plugin was used to place 3 μm circular ROIs on synaptic sites; average intensity measurements over time were measured for each ROI, as described previously[21]. Samples were excluded in the case of motion artifacts in the z plane. Calcium imaging data were further processed in Prism 11 (Graphpad). The first 20 timepoints were averaged to generate an F0 value, and all responses were calculated as ΔF/F0. Presynaptic responses were defined as >20% ΔF/F0 and postsynaptic responses were defined as >5% ΔF/F0. Dot plots in figures represent the average response of all hair bundles or all synaptically active sites within a neuromast. Traces in figures are the average responses of all neuromasts per location or genotype. The max ΔF/F0 was compared between siblings and *ret* mutants or in wild-type animals comparing neuromast location.

Statistical analysis

Statistics were performed in either GraphPad or in RStudio. Paired T-tests were used to compare z-scores for a given gene, Welch's t-test for the number of puncta for gene expression analysis. A one-way ANOVA was used to compare WT hair cell and afferent terminal GCaMP6S ΔF/F response magnitude based on NM location. A 2-way ANOVA was used to compare hair cell counts, synapse counts, synaptic puncta size and afferent terminal response magnitude based on NM location and genotype. Non-parametric data were analyzed using a Wilcoxon rank test.

Computer code

The R code for scRNA-seq analysis is available at https://github.com/anechipor/Nechiporuk-lab-McVay_et_al_2026

Introduction

During nervous system development, neurons must extend their axons and contact distinct peripheral targets. Target-derived neurotrophins and their receptors are well-known mediators of this process. Upon activation, these receptors can signal locally to regulate axon growth cone dynamics. In addition, activated receptors can also be internalized and transported to the cell body via a process termed long-range retrograde signaling. This retrograde communication modulates transcriptional programs to regulate neuronal survival, cell fate, and axon growth. Whether retrograde signaling actively stabilizes neuronal subtype identity and promotes acquisition of subtype-specific functional properties remains poorly understood.

Most of our knowledge about retrograde neurotrophin signaling is derived from studies of the NTRK receptors coupled with secreted NGF or BDNF ligands studied in cultured sympathetic and dorsal root ganglion (DRG) sensory neurons, specifically NTRK1-NGF and NTRK2-BDNF signaling[22]. In sympathetic neurons, NGF/BDNF long-range retrograde signaling promotes the transcription of pro-survival and anti-apoptotic factors[23–25]. Retrograde transport of NTRK1-NGF promotes sensory axon outgrowth[26], while retrograde transport of NTRK2-BDNF is required for dendritic outgrowth in cortical neurons[27].

Similar to NTRK-NGF/BDNF signaling, neurotrophic factor receptor Rearranged during Transfection (RET) and its primary ligand, glial-derived neurotrophic factor (GDNF), play important signaling roles during the development of multiple organ systems. Short-range RET-GDNF signaling plays diverse roles in development, including kidney formation[28,29], survival of sympathetic neurons[30], and specification of the enteric nervous system[29,31]. Long-range RET signaling is required for proper development of motor and sensory neurons[28,32–38]. One long-range transcriptional target, PEA3, is required for motor neuron targeting to the neuromuscular junction[39,40]. In DRG nociceptor neurons, Ret is transcribed in a signaling cascade initiated by NGF [41]. This mechanism is thought to specify general pools of DRG neurons and then long-range interactions with ligands from peripheral targets refine DRG specification through long-range retrograde signaling[42]. NGF in the extracellular environment surrounding unspecialized DRGs is required for subtype maturation, and *Ngf*$^{-/-}$ mutant mice exhibit reduced subtype diversity, likely due to lack of subtype-specific transcription factor localization[43]. While target-derived signaling contributes to neuronal subtype diversification, it remains unknown whether long-range retrograde signaling actively maintains subtype identity and promotes acquisition of the specialized physiological properties that distinguish mature neuronal subtypes.

We utilize the zebrafish posterior lateral line (pLL) to investigate the role of long-range Ret signaling in neuronal subtype specification. The pLL is a mechanosensory system comprised of sensory organs called neuromasts (NMs) positioned along the animal's trunk and peripheral sensory axons that innervate NMs[44–47]. NM organs detect water motion via hair cells and relay signals to the hindbrain to initiate swimming and escape behaviors[44,45]. Development of this sensory system begins in the pLL placode, a transient thickening of the embryonic ectoderm, which gives rise to both the pLL ganglion (pLLg) and the migrating primordium (pLLP)[46,47]. The pLLP migrates caudally, secreting Gdnf[48] and other neurotrophins[49–51], to guide the extending axons of pLL ganglion neurons. We previously identified two transcriptionally distinct neuronal populations within the pLLg: 'pioneers' and 'followers'[5,19]. Pioneers express high levels of the Gdnf receptor *ret*, extend early, and differentiate into neurons with large-caliber axons that preferentially innervate distal NMs. In contrast, followers express low levels of *ret*, extend later by fasciculating with pioneers, and differentiate into neurons with thinner axons that innervate proximal NMs. Distal-targeting pioneer neurons exhibit lower spontaneous firing and input resistance than proximal-targeting follower neurons[52], yet the molecular mechanisms that generate these functional differences remain poorly understood.

Notably, all pLL neuroblasts initially share a 'follower-like' transcriptional ground state; only a subset of neurons upregulates *ntrk1* and *ret* to acquire the pioneer identity[5]. We also showed that Ret signaling is required for pioneer axon extension: in the absence of Ret, pioneer growth cones exhibit reduced complexity, fail to reach the tail, and phenotypically resemble followers[19]. However, the transcriptional targets of Ret-Gdnf signaling and its role in establishing functional subtypes remain unknown.

Here, we combine transcriptional profiling, single-molecule whole-mount in situ hybridization (WISH), single-cell tracing, ultrastructural analysis, and functional calcium imaging to investigate how long-range Ret signaling regulates neuronal subtype maturation in vivo. We show that pioneer neurons are initially specified normally in *ret* mutants but fail to maintain their subtype-specific molecular identity, instead reverting toward a follower-like state. Notably, many hallmark morphological features of pioneer identity, including large-caliber myelinated axons, are preserved in the absence of Ret. In contrast, subtype-specific physiological properties are lost: wild-type pioneer and follower terminals exhibit distinct calcium response profiles, whereas pioneer terminals in *ret* mutants adopt follower-like responses. Collectively, our findings reveal that long-range Ret signaling acts as an instructive mechanism that links maintenance of neuronal subtype identity to acquisition of subtype-specific physiological properties, thereby coupling molecular diversification to functional circuit assembly. Characterizing this mechanism offers new insights into how retrograde

signaling diversifies neuronal function and may inform therapeutic strategies for disorders arising from neurotrophic signaling deficits.

Results and Discussion

scRNA-seq identifies pioneer and follower populations in *ret* mutants

We previously found that pLL pioneers express higher levels of *ret* than followers and that Ret is required for pioneer axon extension[5,19]. We have also shown that Ret long-range retrograde signaling contributes to the growth cone volume and number of filopodia that morphologically distinguishes pioneers from followers[53]. Zebrafish *ret* mutants exhibit pioneer axon terminals with smaller growth cones similar to follower axon terminals[19]. We therefore investigated if long-range retrograde Ret signaling contributes to other molecular differences between pioneers and followers[5]. To test this, we characterized the transcriptional profiles of pLL pioneers and followers in wildtype (WT) and *ret* null mutants (*ret*^{hu2846})[3] using scRNA-seq at 48 hours post-fertilization (hpf), the end of pioneer axon extension. We FAC sorted TgBAC(*neurod1*:*EGFP*)^{nl1}-positive cells to isolate both the CNS and PNS neurons, including pLL neurons[2,5,19]. Following quality control (QC), we analyzed 7,216 WT and 8,011 *ret* mutant cells, from 3 independent replicates per genotype (Fig. 1A). Most of these cells were neurons, with some *neurod1*+ pancreatic cells[54], represented in 40 distinct clusters (Figs. 1A,B and S1). We identified lateral line neurons by expression of known markers *hmx4* and *gfra1b* (Fig. 1C). We then refined this population to just pLL neurons by excluding anterior lateral line neurons (*alcama*+)[55] and differentiating neuroblasts (*neurog1*+)[56]. Both wild-type and *ret* mutant pLL cells subclustered into pioneers and followers (Figs. 1D-E). These data suggest that Ret signaling is not solely responsible for defining pioneer versus follower identity.

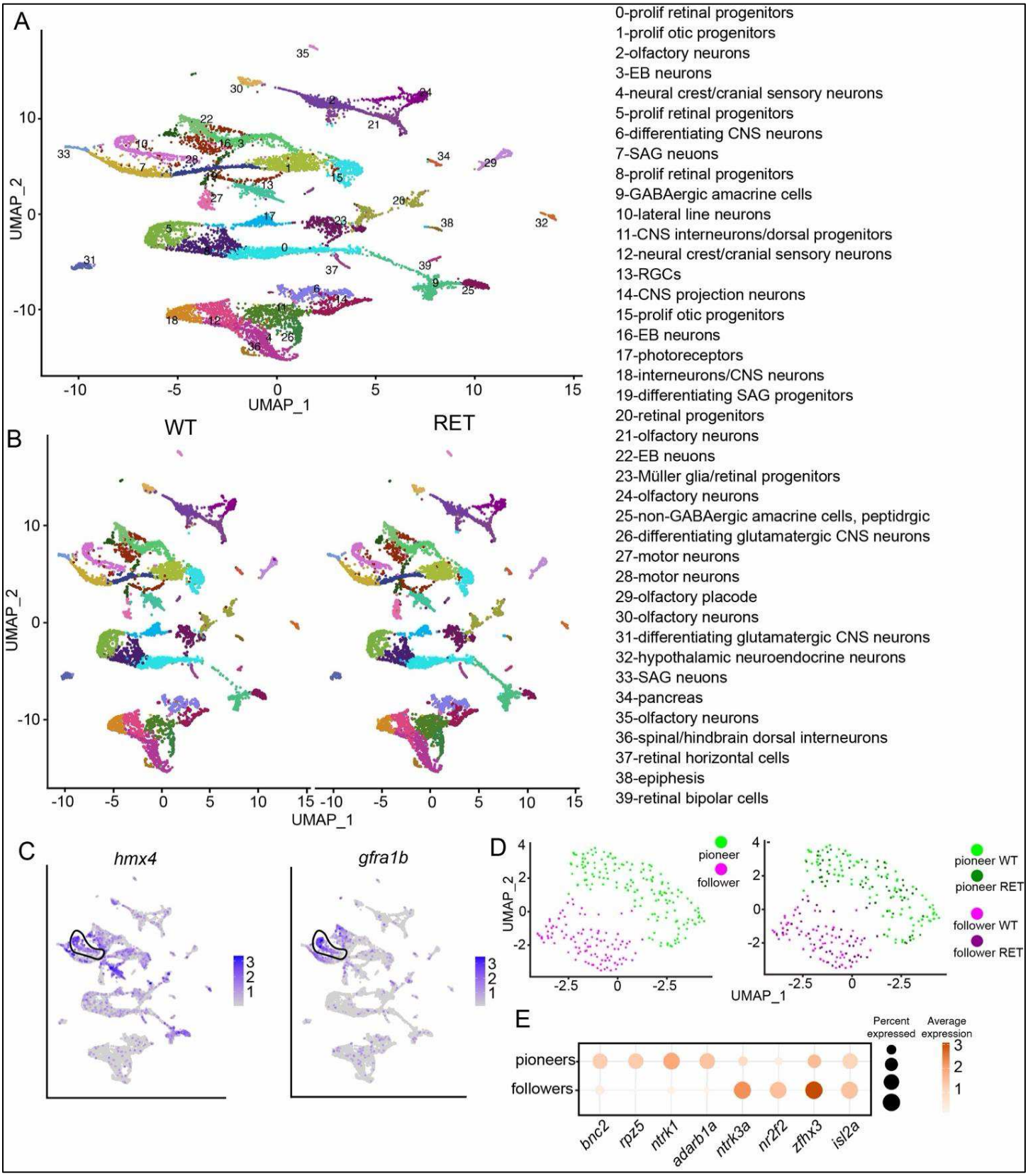


Figure 1: scRNA-sequencing identifies pLL neurons in *ret* mutants and wild-type controls
(A) UMAP of TgBAC(*neurod1:EGFP*)^{nl1}-positive cells at 48 hpf derived from 3 WT and 3 mutant replicas. Cluster annotation is on the right.
(B) Separate UMAPs for WT and mutant cells indicate that all clusters are present in data sets derived from both genotypes.
(C) Feature plots showing expression of lateral line specific markers: *hmx4* and *gfra1b*. Lateral line neurons are outlined.
(D) pLL subclusters into pioneers and followers, with subpopulations present in both the mutant and WT.
(E) Dotplot showing enriched expression of pioneer and follower markers in each subcluster.

Pioneer genes are downregulated, while follower genes are upregulated in *ret* mutant pLL neurons

Although *ret* mutant pLL neurons segregate into pioneers and followers, clustering alone does not exclude substantial transcriptional changes within the pioneer population. To test this, we compared expression of previously defined pioneer and follower markers[5] between WT and *ret* mutant pioneers followed by *in situ* analysis. Our results revealed that pioneer-specific genes were significantly downregulated in the pLL neurons of *ret* mutants compared to WT controls (Fig. 2A,C; average z-scores difference: p=0.009, paired Student's t-test). Reciprocally, pLL neurons in *ret* mutants showed upregulation of several follower genes, indicative of a shift towards a follower-like state, although average z-score difference was not significant (Fig. 2B,C; p=0.134, paired Student's t-test). Overall, these data suggest a shift towards the "follower" state of the *ret* mutant pioneers.

These gene expression differences could arise from failure to maintain pioneer gene expression. Alternatively, retrograde Ret signaling might be required to specify pioneer neuron fate. To distinguish between these scenarios, we performed whole-mount fluorescent *in situ* hybridization (WISH)[17] of the pioneer and follower markers at 22-24 hpf (shortly after pLL neurons are specified) and 48 hpf (end of pioneer axon extension). At 22-24 hpf, both WT and *ret* mutants exhibited the same expression levels of the pioneer genes *adarb1a*, *etv5a*, *gfra1a*, and *bnc2* as well as the follower genes *zfhx3* and *ntrk3a*, indicating pioneer fate is specified normally (Fig. 2D,E and Fig. S2; p=0.6038, 0.3490, 0.6866, 0.1012, 0.4546, and 0.7927, Welch's t-test). In contrast, all 4 pioneer genes were markedly downregulated in *ret* mutants (p=0.006, 0.0032, 0.0031, and 0.0014, Welch's t-test) at 48 hpf (Fig. 2F,G and Fig. S2). Conversely, both follower genes were significantly upregulated in *ret* mutants compared to WT controls (p=0.0035 and 0.0218, Welch's t-test) at this later stage (Fig. 2F,G). These data indicate that while pioneers are specified normally, they fail to sustain their pioneer transcriptional program in *ret* mutants after axon extension. Together, the results support a model in which long-range retrograde Ret signaling is required to maintain pioneer gene expression; in its absence, pioneers partially revert toward a follower-like state.

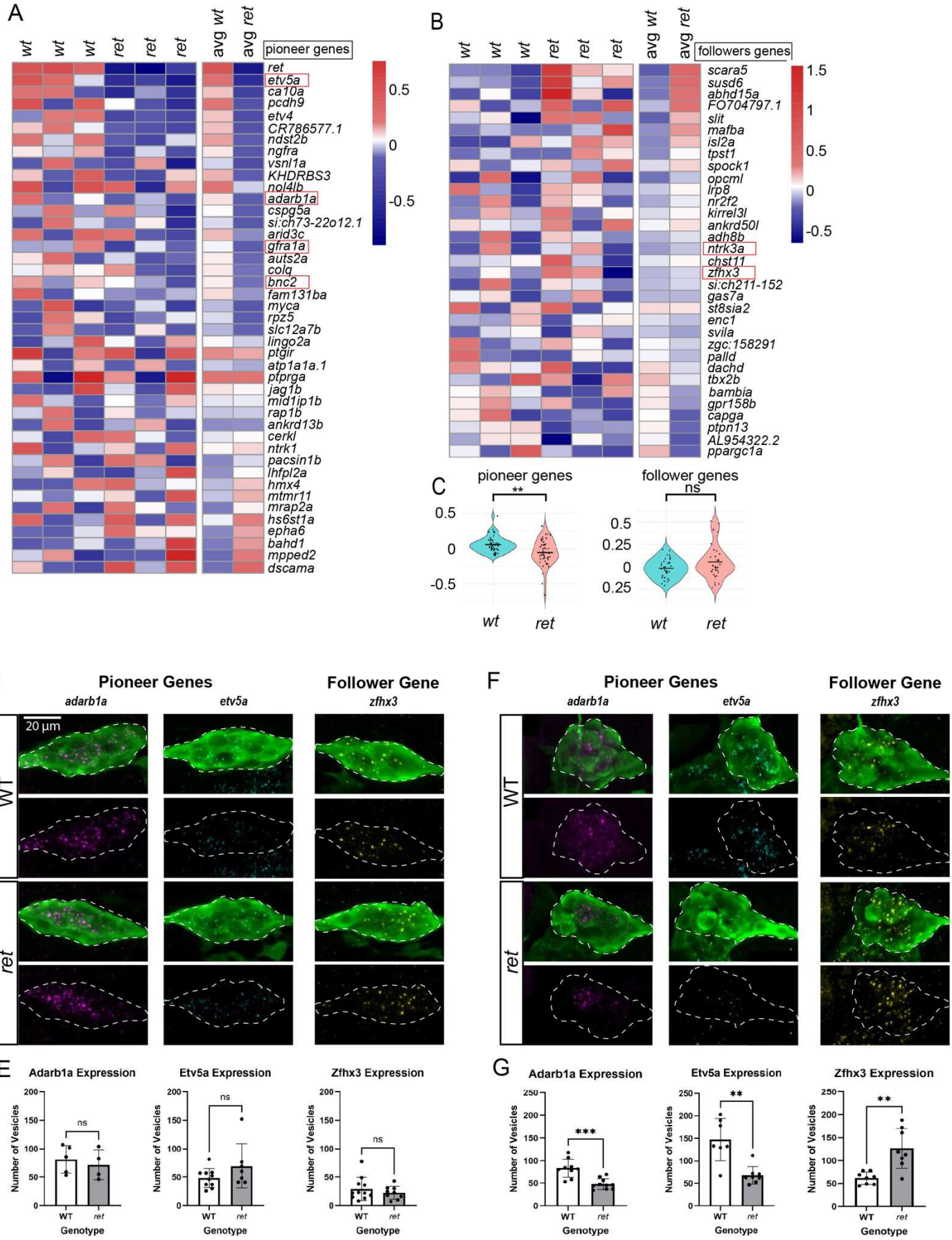

A
wt wt wt ret ret ret avg wt avg ret
pioneer genes
ret
etv5a
ca10a
pcdh9
etv4
CR786577.1
ndst2b
ngfra
vsnl1a
KHDRBS3
nol4lb
adarb1a
cspg5a
si:ch73-22o12.1
arid3c
gfra1a
auts2a
colq
bnc2
fam131ba
myca
rpz5
slc12a7b
lingo2a
ptgir
atp1a1a.1
ptprga
jag1b
mid1ip1b
rap1b
ankrd13b
cerkl
ntrk1
pacsin1b
lhfpl2a
hmx4
mtmr11
mrap2a
hs6st1a
epha6
bahd1
mpped2
dscama
0.5
0
-0.5
B
wt wt wt ret ret ret avg wt avg ret
followers genes
scara5
susd6
abhd15a
FO704797.1
slit
mafba
isl2a
tpst1
spock1
opcml
lrp8
nr2f2
kirrel3l
ankrd50l
adh8b
ntrk3a
chst11
zfhx3
si:ch211-152
gas7a
st8sia2
enc1
svila
zgc:158291
palld
dachd
tbx2b
bambia
gpr158b
capga
ptpn13
AL954322.2
ppargc1a
1.5
1
0.5
0
-0.5
C
pioneer genes
follower genes
**
ns
0.5
0
-0.5
0.5
0.25
0
0.25
wt
ret
wt
ret
D
Pioneer Genes
Follower Gene
adarb1a
etv5a
zfhx3
20 µm
WT
ret
F
Pioneer Genes
Follower Gene
adarb1a
etv5a
zfhx3
WT
ret
E
Adarb1a Expression
Etv5a Expression
Zfhx3 Expression
Number of Vesicles
ns
ns
ns
WT
ret
Genotype
G
Adarb1a Expression
Etv5a Expression
Zfhx3 Expression
Number of Vesicles
***
**
**
WT
ret
Genotype

Figure 2: Pioneer genes are downregulated, while follower genes are upregulated in *ret* mutant pLL neurons at the end of pLL nerve extension.
(A) Heatmap illustrating expression of previously defined pioneer genes in pioneer neurons of WT and *ret* datasets. Note that the average expression of many pioneer genes is downregulated in mutant pLL neurons. Highlighted genes were profiled by WISH.
(B) Heatmap illustrating expression of previously defined follower genes in pioneer neurons of WT and *ret* datasets. Note that the average expression of many follower genes is upregulated in mutant pLL neurons. Highlighted genes were profiled by WISH.
(C) Violin plot illustrating differences in z-scores between all pioneer and follower genes between mutant and WT pioneer neurons. Note that overall pioneer genes are significantly downregulated (***p*=0.009, paired *t*-test), while some follower genes upregulated in mutant cells compare to wild-type controls follower genes (ns - p=0.134; paired *t*-test)
(D) WISH for pioneer (*adarb1a* and *etv5a*) and follower (*zfhx3*) genes at 24 hpf in both WT and *ret* TgBAC(*neurod1*:*EGFP*)+ pLL ganglia.
(E) Quantification of results in D (ns: *p* = 0.6038, 0.3490, and 0.4546, Welch's *t*-test).
(F) WISH for pioneer and follower genes at 48 hpf in both WT and *ret* TgBAC(*neurod1*:*EGFP*)+ pLL ganglia.
(G) Quantification of results in F. Note that pioneer genes are significantly downregulated and follower genes are significantly upregulated in *ret* mutants (***p* = 0.0006, 0.0032, and 0.0035, Welch's *t*-test).

A subset of pLL pioneers extends to innervate distal NMs in *ret* mutants

In *ret* mutants, although most axons do not extend to the tail, this phenotype is not fully penetrant. This incomplete penetrance often results in a less severe truncation of the pLL nerve on one side of the animal. In 60% of all *ret* mutants (6 out of 10 in Fig. S3), the pLL nerve successfully extends to innervate L5 or terminal NMs. These represent the most distal NMs, which are typically targeted by pioneer axons in WT[5,19]. Thus, in *ret* mutants, it is possible that one or more pioneer axon terminals still extends within the pLLP, guided by Ret-independent, secreted cues[5,19,57,49,48,50,51]. Alternatively, follower axons in *ret* mutants may compensate for the loss of the pioneer scaffold and extend independently to innervate distal NMs.

To distinguish between these scenarios, we transiently labeled individual pioneer neurons in *ret* and WT animals. This allowed us to track pioneer axons during and after extension to address whether they eventually innervate distal NMs. TgBAC(*neurod1*:*EGFP*)^{nl1} embryos were injected with *pDestTol2-hsp70-mCherry-SILL* plasmid and sorted for embryos that exhibited labeling of one or two pLL neurons (Fig. 3A-B). These embryos were then imaged at 24 hpf, to determine if the labeled neuron was a pioneer (defined as having an axon terminal within the pLLP). Importantly, although pioneer neurons later exhibit a partial shift toward a follower-like transcriptional state, pioneer and follower marker expression is preserved at 24 hpf in *ret* mutants, indicating that neurons with axon terminals in the pLLP at this stage are bona fide pioneers. We then imaged the same embryos at 72 hpf to assay pioneer neuron targets (Fig. 3A,B). In WT siblings, most (22 out of 24) pioneer neurons innervated distal NMs, as previously reported[5,19] (Fig. 3C,E; Suppl. Table 1). In *ret* mutants, 3 out of 6 labeled pioneer axons extended and innervated distal NMs (evident by stereotyped elaboration of axon terminals; Fig. 3D,F; Suppl. Table 1). These data indicate that a subset of pLL pioneer axons can extend and innervate distal NMs in *ret* mutants.

To further test if the axons extending to distal NMs in *ret* mutants were pioneers, we examined their morphology more closely. Previous studies showed that axons innervating distal NM display a larger caliber and a higher level of myelination compared to those innervating proximal NMs[5,19,58–60]. To test if these features are present in *ret* mutants, we used transmission electron microscopy (TEM) to visualize the pLL nerve near L5 NMs in *ret* mutants and WT siblings (Fig. S4A-E). While we observed a reduction in myelinated axons in *ret* mutants compared to WT siblings (average of 3 in WT vs. 1 in mutant; p=0.0393, Wilcoxon rank-sum test; Fig. S4C,D), large caliber myelinated axons were still present at distal L5 NMs near the animal's tail (Fig. S4B). The area of myelinated axons was not different between WT siblings and *ret* mutants (Fig. S4E; p=0.1026, Wilcoxon rank-sum test). We did not observe a difference in the number or area of small unmyelinated axons in WT siblings compared to *ret* mutants (Fig. S4D,E). These results suggest that in *ret* mutants, similar to WT siblings, pioneers that extend their axons differentiate into neurons with large caliber myelinated axons.

Overall, although the *ret* mutant phenotype is incompletely penetrant, our single-neuron labeling and TEM analysis show that at least a subset of pioneer neurons in *ret* mutants still extend to and innervate distal neuromasts. Together with our single-cell transcriptomic and WISH data, these observations argue that residual distal innervation is mediated by pioneers rather than compensatory extension by followers. This is consistent with our previous observation that pLL follower axons cannot extend in the absence of pioneers[5]. Nonetheless, the reduced frequency of such events and the molecular failure of pioneers to maintain their transcriptional program indicate that long-range Ret signaling is normally required for robust maturation and function of the pioneer population.

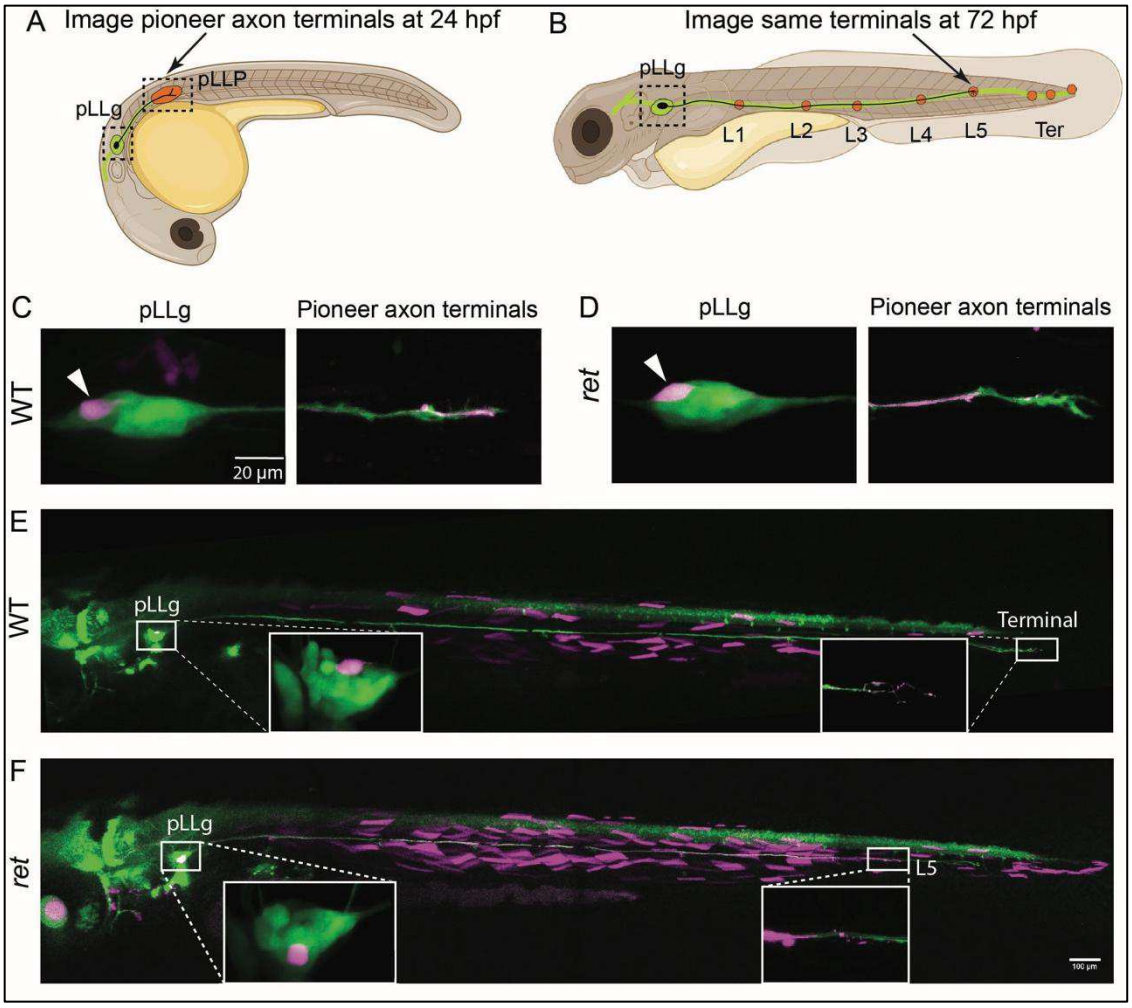


Figure 3: pLL pioneers extend to innervate distal neuromasts in the *ret* mutant.
(A,B) Diagrams describing the experimental set up. Animals carrying TgBAC(*neurod1:EGFP*)^{nl1} transgene to visualize pLL nerve were injected with *pDestTol2-hsp70-mCherry-SILL* plasmid to mark 1-2 pLL neurons and their axons. Pioneer neuron cell body and its terminal were imaged at 24 hpf (A) and then same animal was imaged at 72 hpf (B) to determine the innervation target.
(C) Confocal images of the pLLg and pioneer axon terminal in a WT at 24 hpf. Arrowhead marks labeled neuron.
(D) Confocal images of the pLLg and pioneer axon terminals in the *ret* mutant at 24 hpf. Arrowhead marks labeled neuron.
(E) Tiled, confocal image of the same WT embryo at 72 hpf show innervation of the L5 NM.
(F) Tiled, confocal image of the same *ret* mutant injected shows innervation of the L5 NM.

Calcium responses in afferent terminals are less sensitive at more distal locations

NM targeting in the pLL is determined by neuroblast delamination timing, with pioneer neurons preferentially innervating the most distal NMs (L4, L5 and termNMs) and followers targeting more proximal ones[5] (Fig. 3A). Previous neurophysiological studies measured at the cell soma have shown that early-extended, large-caliber pLL neurons (pioneers) are less excitable and exhibit lower spontaneous firing rates compared to later-extended, more proximal small-caliber neurons[60]. Furthermore, stimulation of distal NMs (L5), but not proximal ones, reliably elicits fictive escape behaviors[60]. However, whether these physiological distinctions arise at the post-synaptic terminals remain unknown.

To address this, we analyzed post-synaptic calcium responses in the afferent terminals of WT animals harboring a Tg(*en.sill,hsp70l:GCaMP6s*)^{idc8} transgene that expresses GCaMP6s in pLL neurons[7] (Fig. 4A,B). Upon stimulating NM hair cells for 2 or 0.5 seconds with a calibrated fluid jet[60], we observed that afferent terminals innervating proximal NMs (L1, L2) exhibited significantly higher evoked calcium responses compared to those innervating distal NMs (L5, terminal) (Fig. 4C-G; *p* values varied between 0.05 and 0.001 for L1/L2 vs. L5/termNM, one-way ANOVA). This suggests that the sensitivity of the afferent terminal varies based on its target location.

To determine if these postsynaptic differences stem from presynaptic variability, we examined evoked presynaptic calcium responses in hair cells using a Tg(*myo6b:memGCaMP*)^{idc1} [61] transgenic (Fig. S5A,B). We observed no difference in evoked presynaptic calcium signals in hair cells between L2, L5, and termNMs (Fig. S5C-E; p=0.7281 L5, p=0.8627 term, one-way ANOVA). This indicates that presynaptic variation does not account for the postsynaptic differences observed between proximal and distal NMs.

We next assessed whether differences in synapse number or size of pre- and post-synaptic structures could account for the postsynaptic differences between proximal and distal NMs. To examine synapses, we quantified pre- and post-synaptic puncta using antibodies against pan-CTBP and pan-MAGUK, respectively (Fig. S6A, C-F). In controls NMs, we found no significant differences in synapse number or the size of pre- and post-synaptic compartments between proximal and distal NMs (Fig. S6C-F; comparison to L2: synapse number p=0.2956 L5, p=0.9509 terminal; presynapse size p=0.9668 L5, p=0.9706 terminal; postsynapse size p=0.8985 L5, p=0.1665 termNM, one-way ANOVA). In addition, no difference in synapse number or size was observed between sibling and *ret* mutant NMs based on NMs location (Fig. S6C-F; synapse number p=0.8257 L2, p=0.9990 L5, p=0.0691 terminal; presynapse size p=0.9120 L2, p=0.8388 L5, p=0.2338 termNM; postsynapse size p=0.9842 L2, p=0.7838 L5, p=0.8959 terNM, two-way ANOVA). These results indicate that

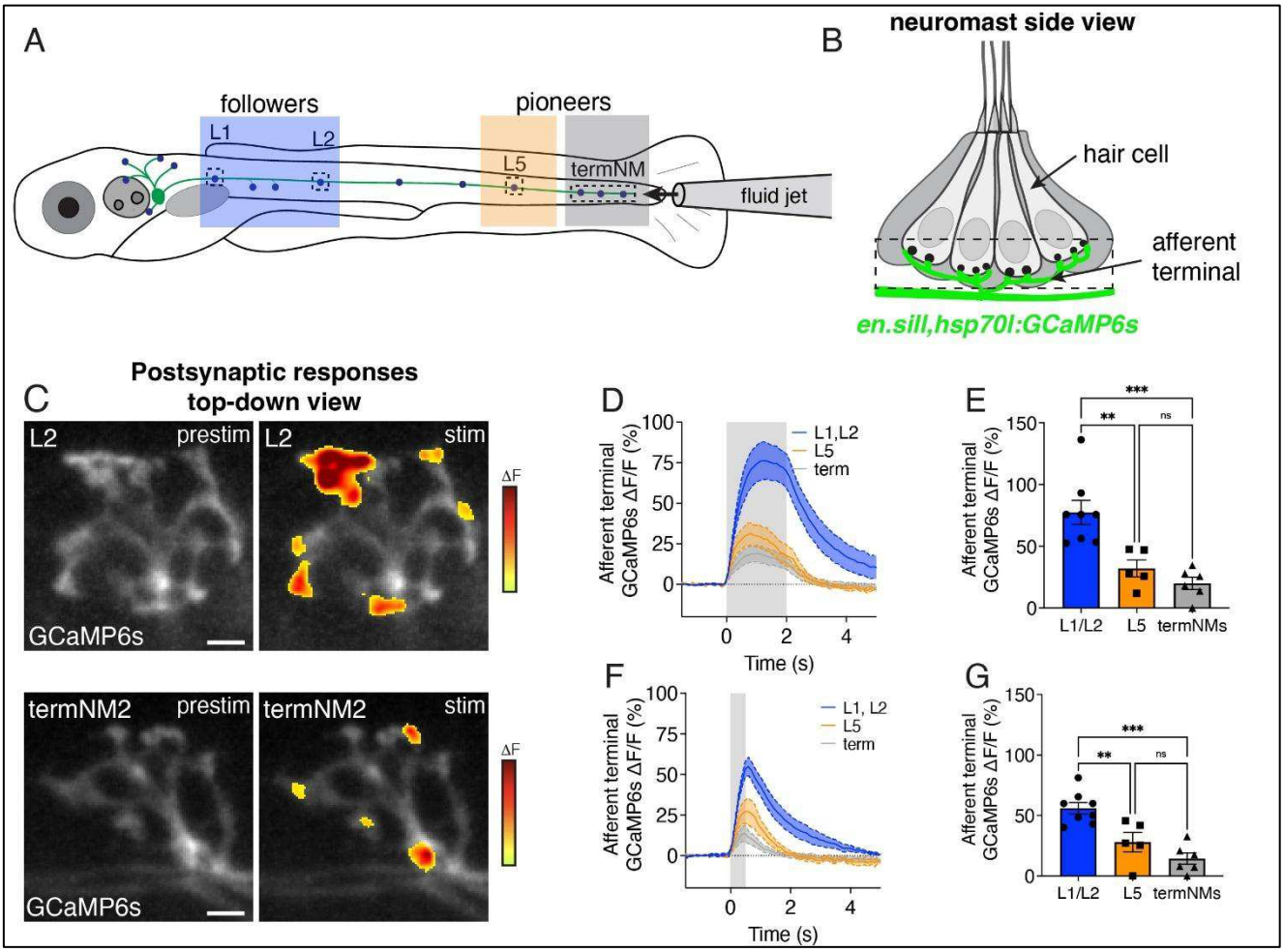


Figure 4: Calcium responses in afferent processes are less sensitive in more terminal neuromasts.
(A) Diagram of fluid jet experimental set up to stimulate NMs at different locations along the pLL.
(B) Anatomy of the pLL NM, identifying the location of *hsp70l:GCaMP6s* in the afferent terminal.
(C) Example image of post-synaptic responses from the proximal L2 and terminal (term) NM2 before and after fluid-jet simulation. Increases in GCaMP6s signals are encoded according to the heatmaps.
(D) Average traces of afferent terminal postsynaptic responses for proximal L1/L2 NMs (blue), and distal L5 NMs (orange), and terminal NMs (grey) during a 2-second fluid-jet stimulation marked by grey rectangle.
(E) Quantification of the average magnitude per NM used to generate the average traces results in (D).
(F) Average traces of afferent terminal postsynaptic responses for the L1/L2 NMs (blue), L5 NMs (orange), and terminal NMs (grey) followed during a 0.5-second fluid-jet stimulation marked by grey rectangle.
(G) Quantification of the average magnitude per NM used to generate the results in (F).
N = 5-6 WT animals and N = 8 L1/L2, 5 L5 and 6 termNMs, (* p<0.05, ** <0.01, *** <0.001, one-way ANOVA). The scale bar in C = 5 µm.

gross variations in synapse size or number do not account for the postsynaptic differences observed between proximal and distal NMs.

Taken together, these results show that the differential calcium responses observed between proximal and distal NMs are not driven by hair cell activity or synaptic abundance but rather reflect distinct intrinsic properties of the post-synaptic afferent terminals. This functional tuning supports a model where distal NMs, innervated by high-threshold pioneers, are tuned for large flow changes to trigger escape responses, while proximal NMs detect subtle flow for positioning in the water[52].

Ret controls differences in afferent calcium response in distal neuromasts

Given the transcriptional shift observed in *ret* mutant pioneers towards a follower-like profile, we investigated whether their functional properties were similarly altered. In contrast to WT controls, *ret* mutants showed no significant difference in calcium responses between distal (L5) and proximal (L2) NMs (Fig. 5A-E; L2 versus L5 terminals in *ret* mutants, p=0.6804, two-way ANOVA). Strikingly, distal (L5) terminals in *ret* mutants exhibited high-amplitude calcium signals that were significantly larger than those in WT L5 terminals (Fig. 5A-E; L5 terminal response, p=0.0348, two-way ANOVA). Instead, the L5 terminals responses in *ret* mutants were not significantly different from the responses of WT proximal (L2) terminals, effectively abolishing the physiological distinction between these two functional subtypes (Fig. 5A-E; L2 sibling versus L5 *ret* mutant terminal response, p=0.5858, two-way ANOVA). As established above, synapse number and size in *ret* mutant L5 NMs remained comparable to WT controls (Fig. S6A-F), indicating that this functional alteration is not driven by changes in synaptic connectivity. Collectively, these data suggest that Ret signaling is necessary to drive the pioneer-specific transcriptional program; in its absence, pioneer neurons fail to acquire their distinct physiological identity, instead retaining a default, high-sensitivity 'follower-like' state.

Although retrograde trophic signaling has long been implicated in neuronal differentiation and structural maturation, direct links between long-range retrograde signaling and the consolidation of subtype-specific transcriptional programs and synaptic function in vivo remain limited. By integrating single-cell transcriptomics, single-molecule WISH, single-cell tracing, ultrastructural analysis, and physiological assays, we show that long-range Ret signaling is not required for initial pioneer specification but is essential for maintaining the pioneer transcriptional program and for structural and functional maturation of pioneer synapses in the zebrafish pLL. Loss of Ret causes pioneers to partially revert toward a follower-like molecular state and abolishes their distinctive synaptic physiology, arguing that retrograde Ret signaling reinforces neuronal identity and sculpts circuit function. To our knowledge, this is the first *in vivo* demonstration that long-range retrograde signaling is required to sustain a defined transcriptional program and to consolidate the functional maturation of a specific neuronal subtype. Finally, among candidate Ret effectors, *adarb1a*, a zebrafish homolog of the neuronal adenosine-to-inosine (A-to-I) RNA-editing enzyme *ADAR2*, is particularly compelling. ADAR2-dependent editing can recode ion channels (notably AMPA receptor subunits[62–64]) and thereby alter calcium homeostasis and excitability. Defining whether Adarb1a and A-to-I editing act downstream of Ret to drive pioneer maturation will be an important next step to connect retrograde signaling with post-transcriptional control of neuronal function.

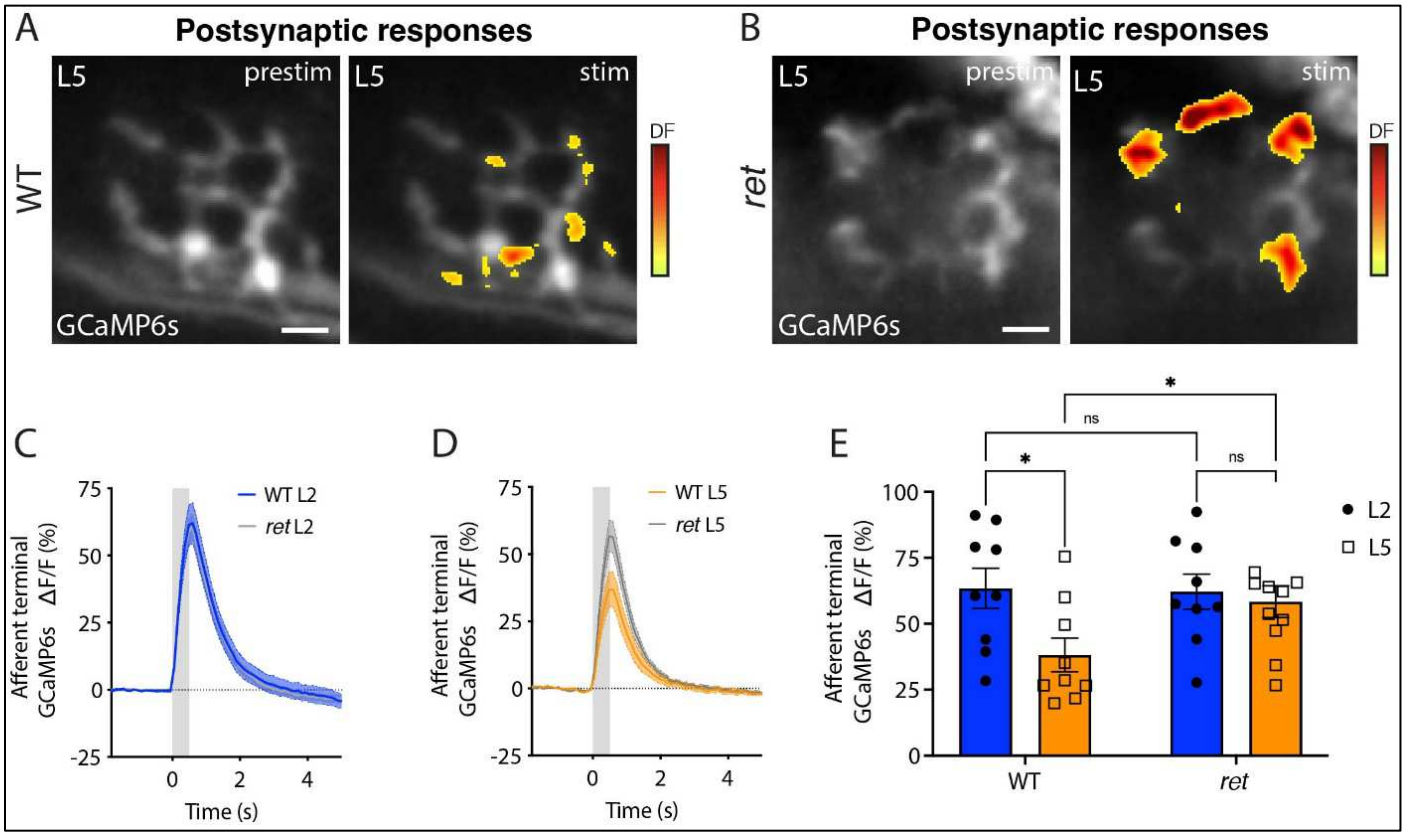


Figure 5: Ret controls differences in afferent calcium response in distal neuromasts.
(A) Example image of post-synaptic responses in a WT L5 NM before and after fluid-jet simulation. Increases in GCaMP6s signals are encoded according to the heatmap.
(B) Example image of post-synaptic responses in a *ret* mutant L5 NM before and after fluid-jet simulation.
(C) Average traces of WT (blue) and *ret* mutant (grey) afferent terminal postsynaptic responses in L2 NMs during a 0.5-s fluid-jet stimulation marked by the grey bar.
(D) Average traces of WT (orange) and *ret* mutant (grey) afferent terminal postsynaptic responses in L5 NMs during a 0.5-s fluid-jet stimulation marked by the grey bar.
(E) Quantification of the average magnitude per NM used to generate the average traces in (C) and (D). While WT animals show lower postsynaptic responses in distal L5 NMs compared to more proximal L2 NMs, in *ret* mutants postsynaptic response magnitudes are not different in proximal and terminal NMs. Postsynaptic response magnitude is not different in proximal NMs in WT and *ret* mutants.
N = 9 WT and *ret* animals, (*p<0.05, two-way ANOVA). The scale bar in A and B = 5 µm.

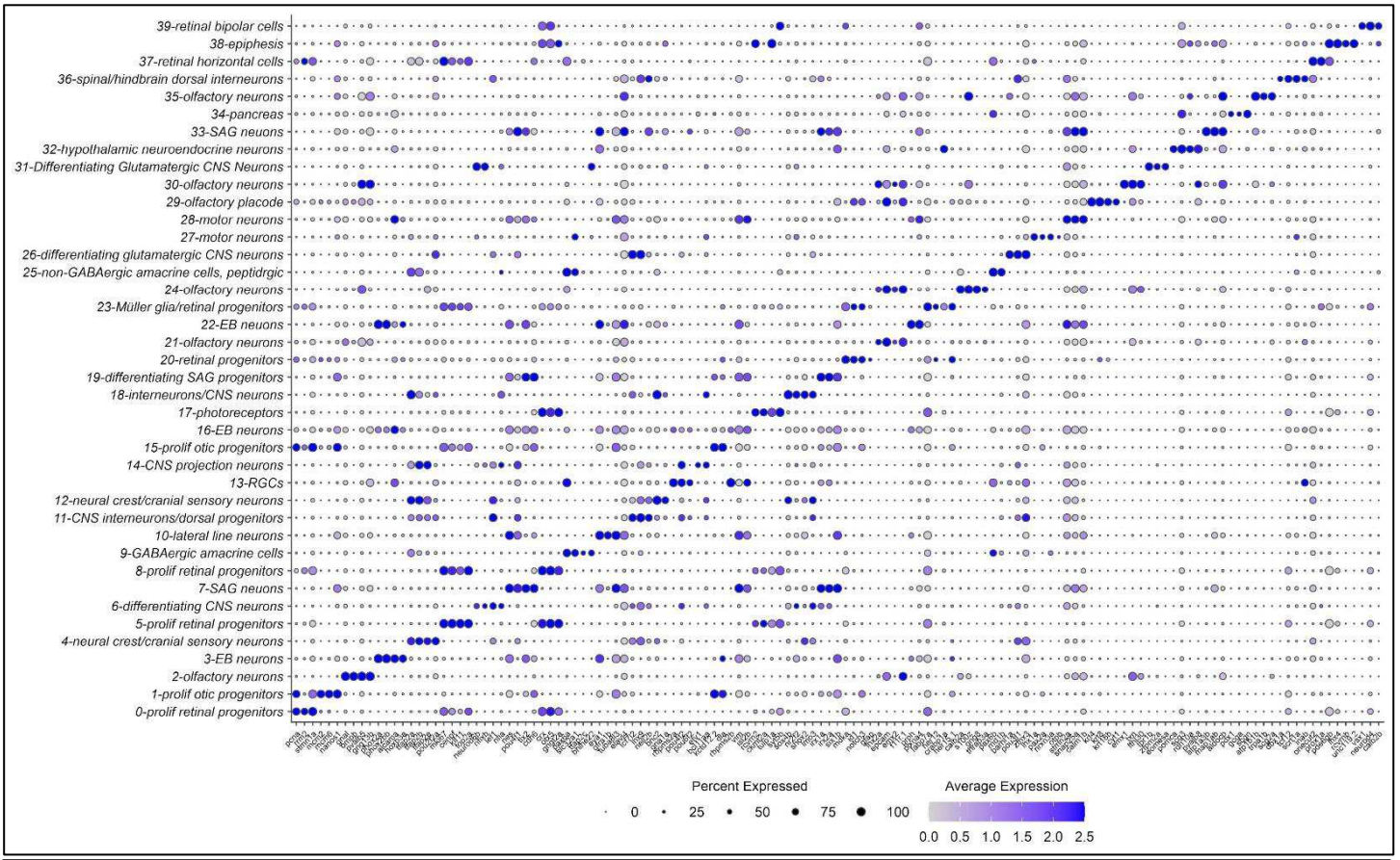
Supplemental Information

Supplemental Table 1.

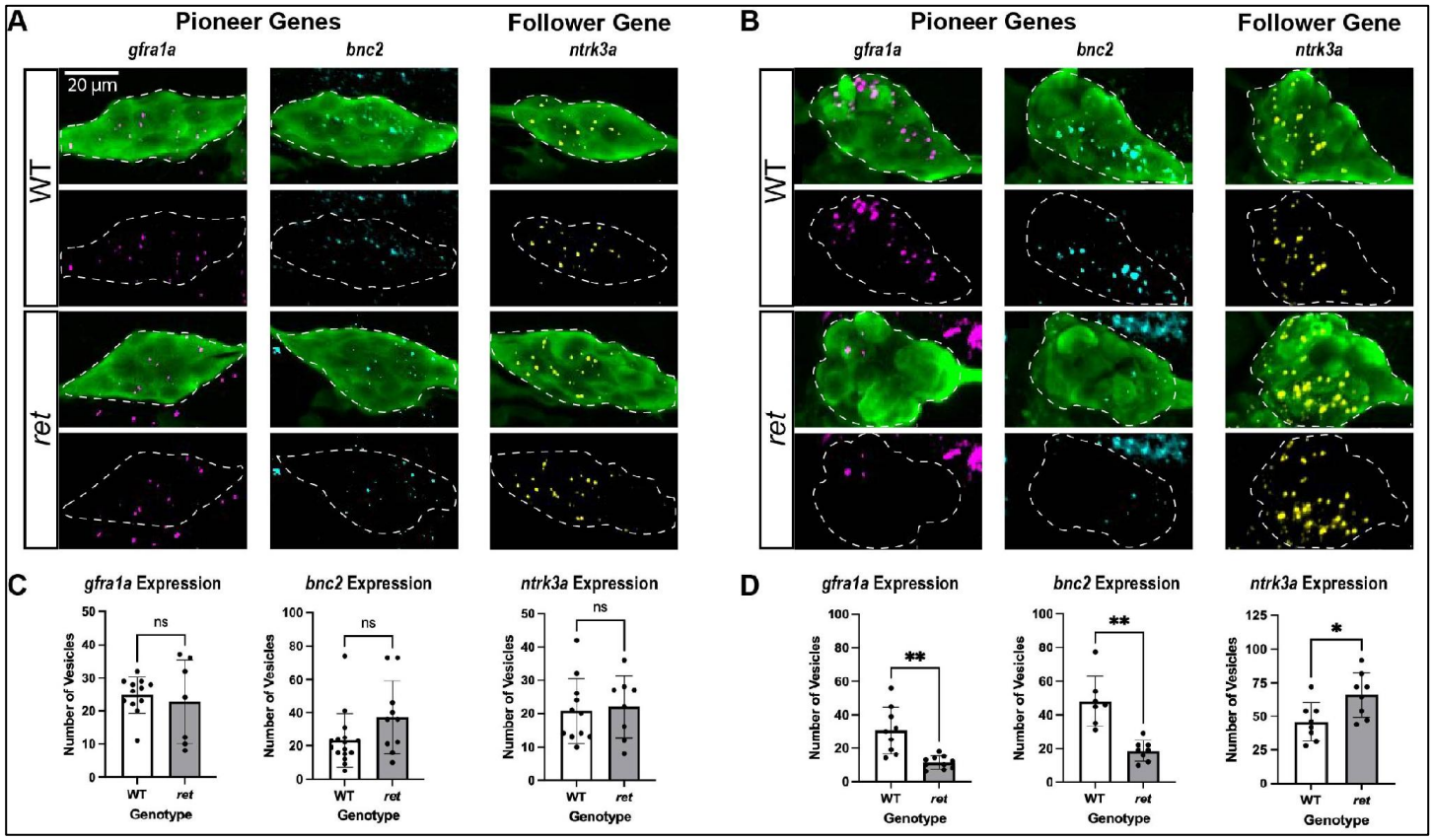
Sample number	Genotype	Pioneer position at 24 hpf	Neuromast target at 72 hpf
1	*ret*	Trailing	L1
2	*ret*	Leading	L5
3	*ret*	Trailing	Truncated before L5
4	*ret*	Trailing	L5
5	*ret*	Trailing	No neuromast innervation, truncated around L3
6	*ret*	Trailing	L4
7	Het	Trailing	Terminal neuromasts
8	Het	Trailing	Terminal neuromasts
9	Het	Trailing	L4
10	Het	Trailing	Terminal neuromasts
11	Het	Trailing	L4
12	Het	Trailing	Terminal neuromasts
13	Het	Trailing	Terminal neuromasts
14	Het	Trailing	Terminal neuromasts
15	Het	Trailing	Terminal neuromasts
16	Het	Trailing	L4
17	Het	Trailing	No neuromast innervation, mCherry expression extends almost to terminal neuromasts
18	Het	Trailing	L5
19	Het	Trailing	Terminal neuromasts
20	Het	Trailing	Terminal neuromasts
21	Het	Leading	Innervated L2, truncated
22	Het	Leading	Terminal neuromasts
23	WT	Trailing	L5
24	WT	Trailing	Terminal neuromasts
25	WT	Trailing	Terminal neuromasts
26	WT	Trailing	Terminal neuromasts
27	WT	Leading	Terminal neuromasts
28	WT	Trailing	L5
29	WT	Trailing	Terminal neuromasts
30	WT	Trailing	Terminal neuromasts
31	WT	Leading	Innervated L3, truncated before L4

Supplemental Table 1. Pioneer axon terminals innervates distal NMs in *ret* mutants.
Summary of pLL pioneer axon extension in all TgBAC(*neurod1*:*EGFP*)^{nl1}+ *ret* mutants and wild-type siblings injected with *pDestTol2-hsp70-mCherry-SILL* and grouped by genotype. Note that 3 (highlighted) out of 6 mutant pioneer axons innervated distal NMs (L4 and L5). Leading pioneers defined as the most caudal terminal within the migrating pLLP, whereas trailing are all other pioneers within the pLLP. Het = heterozygous, WT = wildtype.

Supplemental Figures



Supplemental Figure 1. scRNA-seq of TgBAC(*neurod1:EGFP*)^{nl1}-positive cells identifies both CNS and PNS populations of neuron.
Expression of genes used to identify individual clusters in the UMAP plot shown in Figure 1A. Abbreviations: EB – epibranchial neurons; RGC – retinal ganglion cells; SAG – statoacoustic ganglion.



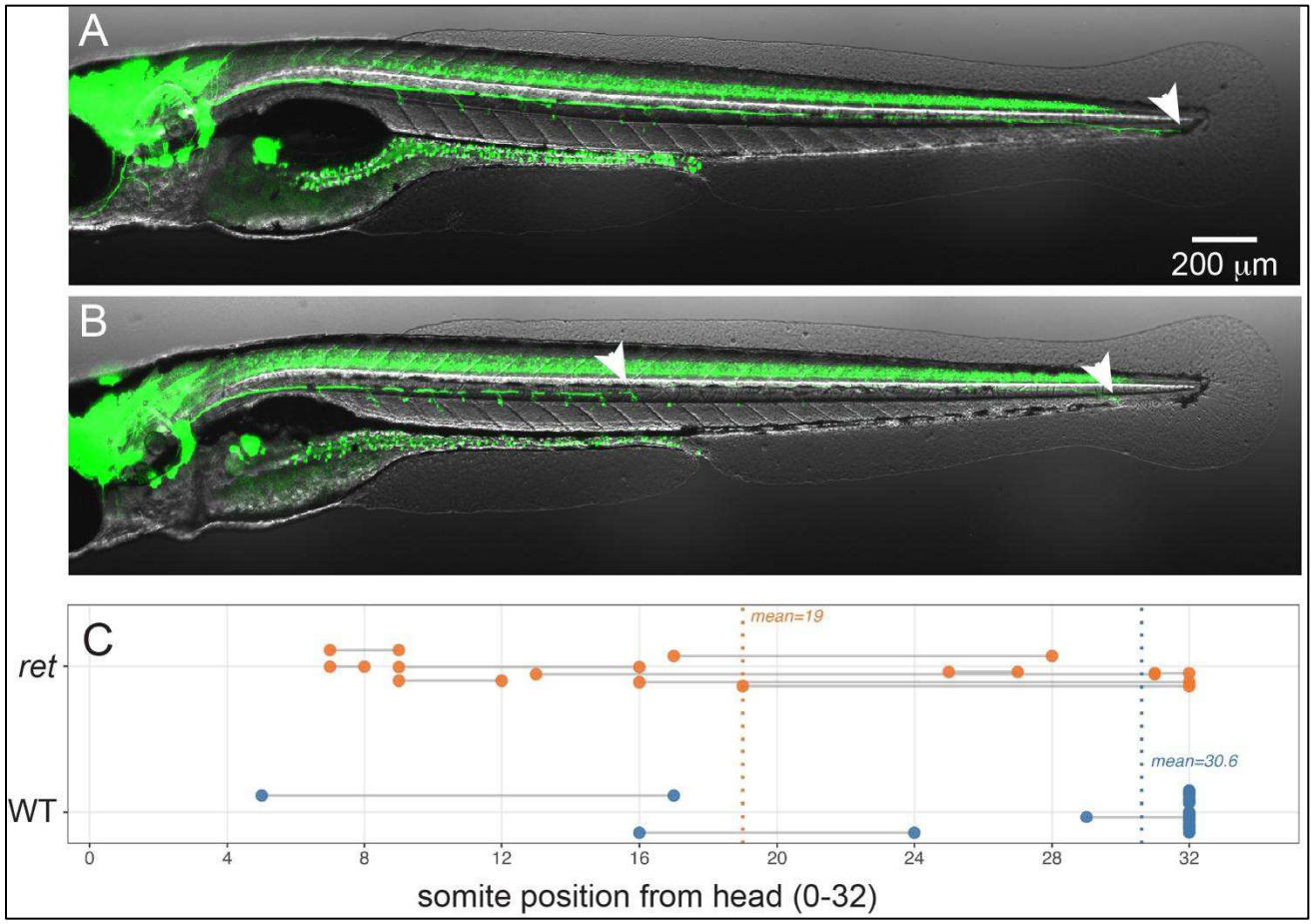
Supplemental Figure 2: Pioneer genes are downregulated, while follower genes are upregulated in *ret* mutant pLL neurons.

(A) WISH for pioneer (*gfra1a* and *bnc2*) and follower (*ntrk3a*) genes in both WT and *ret* TgBAC(*neurod1*:*EGFP*)+ pLL ganglia at 24 hpf.

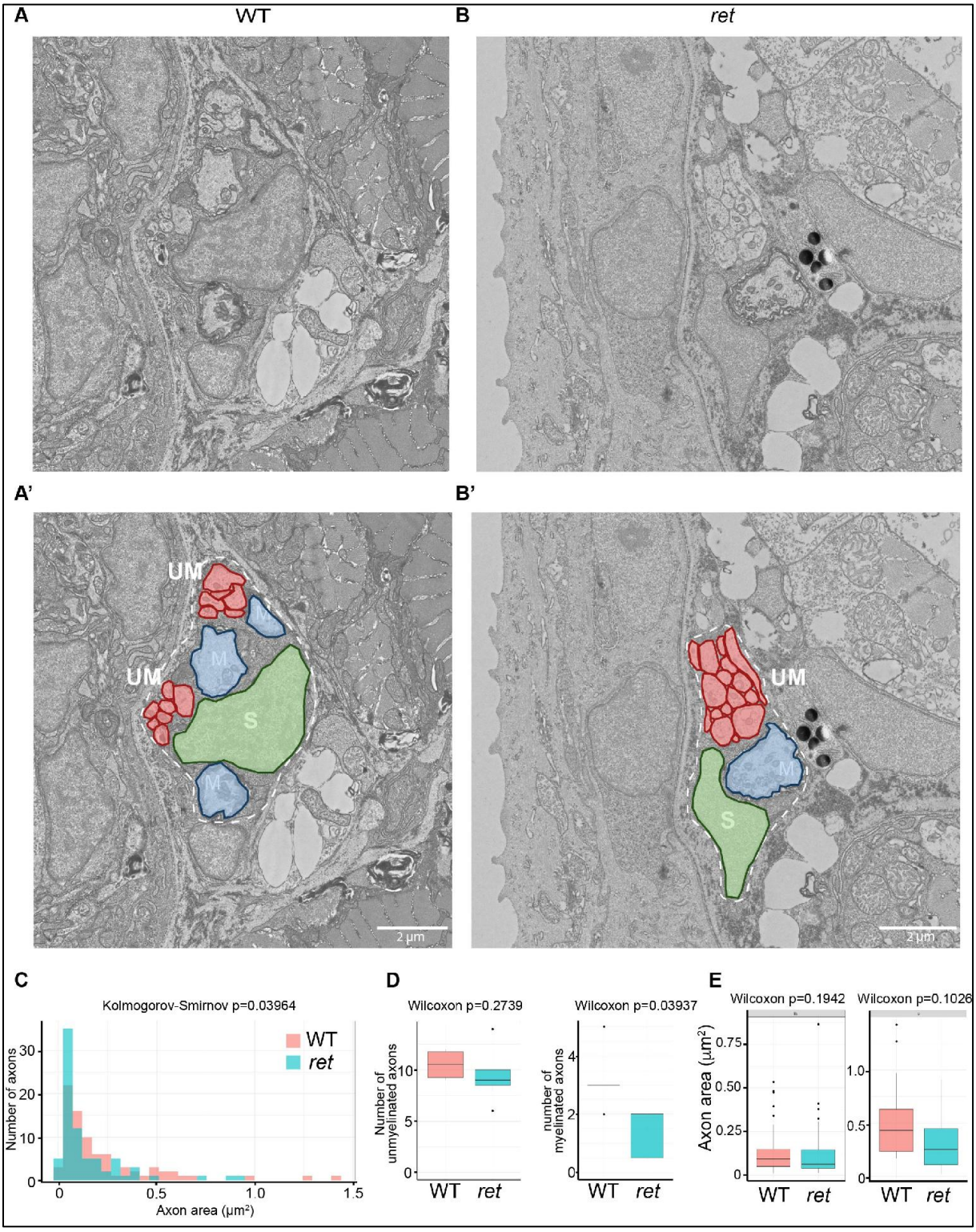
(B) Quantification of results in A (ns: p = 0.6866, 0.1012, and 0.7927, Welch's t-test).

(C) WISH for pioneer (*gfra1a* and bnc2) and follower (*ntrk3a*) genes at 48 hpf in both WT and *ret* TgBAC(*neurod1*:*EGFP*)+ pLL ganglia.

(D) Quantification of results in C. Note that pioneer genes are significantly downregulated and follower genes are significantly upregulated in *ret* mutants (p = **0.0031, **0.0014, and *0.0218, Welch's t-test).

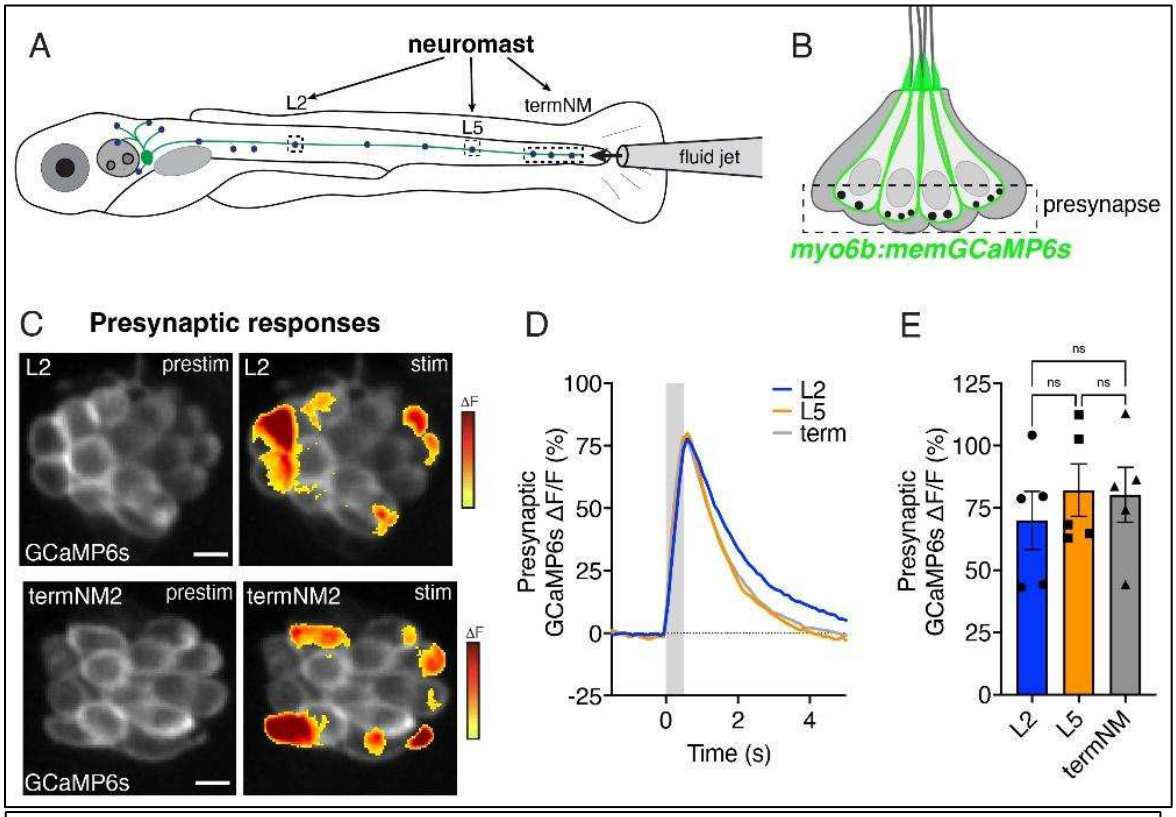


Supplemental Figure 3. *ret* mutants exhibit a semi-penetrant pLL axon truncation. TgBAC(*neurod1:EGFP*)^{nl1} zebrafish larvae at 96 hpf in a WT (A) and *ret* mutant (B) background. *ret* mutants exhibit varying degrees of axon truncation in the pLL, but most larvae exhibit some axons fully extending and innervating distal (L5 and ter) NMs. White arrows indicate axon terminals. C) Quantification of axon extension in *ret* mutants (orange) and WT siblings (blue) relative to somite position.

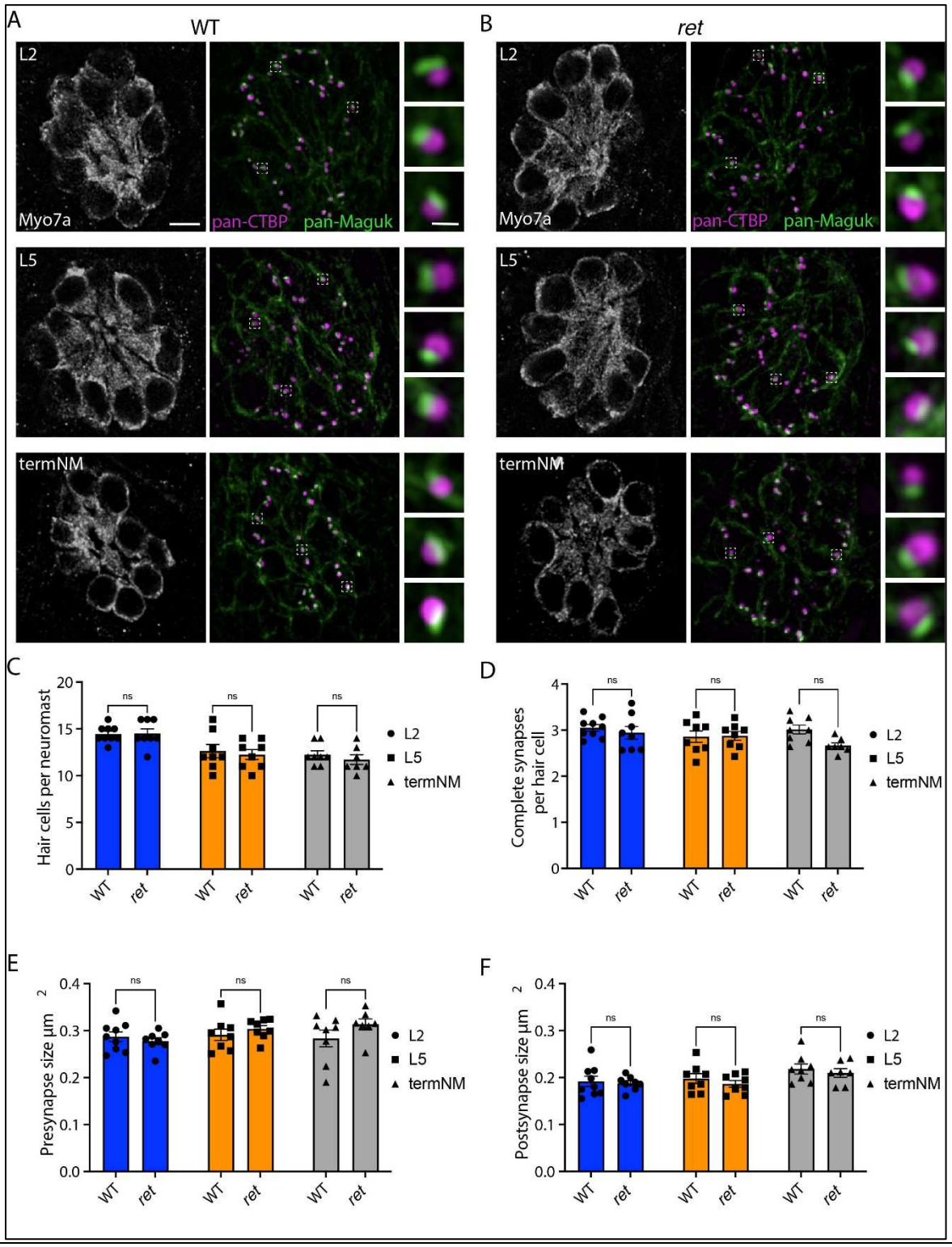


24

Supplemental Figure 4. Distal part of pLL nerve in the *ret* mutant contains myelinated axons.
(A,B) Transmission electron micrographs from a wild-type sibling, pseudocolored in A', and *ret* mutant tails (around L5; pseudocolored in B') at 4 dpf demonstrate presence of myelinated and unmyelinated axons. Lateral line nerve is outlined with a dashed line.
(C) Histogram showing area distribution of pLL axon in *ret* mutants and wild-type siblings. Note that *ret* mutants have fewer large axons (Kolmogorov-Smirnov p=0.03964).
(D) *ret* mutants and wild-type siblings have similar number of unmyelinated axons (Wilcoxon p=0.2739), but fewer myelinated axons (Wilcoxon p=0.03937).
(E) Axon area is not changed in either unmyelinated or myelinated axons in the pLL nerve of ret mutants (unmyelinated: Wilcoxon p=0.1942; myelinated: Wilcoxon p=0.1026).
Abbreviations: M, myelinated axon (blue); UM, unmyelinated axons (red); S, Schwann cell (green).



Supplemental Figure 5: Proximal and distal neuromast HCs respond similarly to stimulation.
(A) Diagram of fluid-jet experimental set up to stimulate NMs and different locations and measure pLL HC calcium activity.
(B) NM anatomy highlighting the HC presynaptic imaging plane (dashed box). Green indicated where membrane-localized GCaMP6s, *myo6b:memGCaMP6s* is localized.
(C) Example images of HC presynaptic responses in L2 and terminal NM2 in WT animals before and after fluid-jet simulation. Increases in GCaMP6s signals are encoded according to the heatmaps.
(D) Average traces of HC presynaptic responses in L2 (blue), L5 (orange) and terminal NMs (grey) during a 0.5-second fluid-jet stimulation marked by grey rectangle.
(E) Quantification of the average response magnitude per NM used to generate the traces in (D). In WT animals the HC presynaptic responses do not differ between NM location.
N = 5 WT animals, (ns = not significant, one-way ANOVA). The scale bars in C = 5 μm.



Supplemental Figure 6: Number of synaptic puncta is not different between proximal and distal NMs in both wildtypes and *ret* mutants.

(A) Immunolabeling of L2, L5, and terminal NM synapses in WT embryos at 5 dpf. Myo7a (white) labels HCs, CTBP labels presynapses, and MAGUK labels postsynapses.

(B) Same immunolabeling of L2, L5, and terminal NM synapses as (A) in *ret* mutants.

(C) Quantification of the number of HCs in L2, L5, and terminal NMs. The number of HCs does not differ between WT and *ret* mutant embryos.

(D) Quantification of the number of complete synapses per HC in L2, L5, and terminal NMs. The number of synapses per HC does not differ between WT and *ret* mutant embryos.

(E-F) Quantification pre- and post-synapse size in L2, L5, and terminal NMs in WT and *ret* mutants. Sizes do not differ between NM locations or between genotypes.

N = 7-9 WT or *ret* animals, (ns = not significant, two-way ANOVA). The scale bars in A = 5 µm and 0.5 µm in the inset.

Works Cited

1. Kimmel, C. B., Ballard, W. W., Kimmel, S. R., Ullmann, B. & Schilling, T. F. Stages of embryonic development of the zebrafish. *Dev. Dyn. Off. Publ. Am. Assoc. Anat.* **203**, 253–310 (1995).
2. Obholzer, N. *et al.* Vesicular Glutamate Transporter 3 Is Required for Synaptic Transmission in Zebrafish Hair Cells. *J. Neurosci.* **28**, 2110–2118 (2008).
3. Knight, R. D. *et al.* Ret signalling integrates a craniofacial muscle module during development. *Development* **138**, 2015–2024 (2011).
4. Haas, P. & Gilmour, D. Chemokine Signaling Mediates Self-Organizing Tissue Migration in the Zebrafish Lateral Line. *Dev. Cell* **10**, 673–680 (2006).
5. Woodruff, B. M. *et al.* Axon targeting of transcriptionally distinct pioneer neurons is regulated by retinoic acid signaling. *Nat. Commun.* **16**, 5747 (2025).
6. Valera, G. *et al.* A neuronal blueprint for directional mechanosensation in larval zebrafish. *Curr. Biol.* **31**, 1463-1475.e6 (2021).
7. Zhang, Q. *et al.* Synaptically silent sensory hair cells in zebrafish are recruited after damage. *Nat. Commun.* **9**, 1388 (2018).
8. Covassin, L. *et al.* Global analysis of hematopoietic and vascular endothelial gene expression by tissue specific microarray profiling in zebrafish. *Dev. Biol.* **299**, 551–562 (2006).
9. Hao, Y. *et al.* Integrated analysis of multimodal single-cell data. *Cell* **184**, 3573-3587.e29 (2021).
10. Satija, R., Farrell, J. A., Gennert, D., Schier, A. F. & Regev, A. Spatial reconstruction of single-cell gene expression data. *Nat. Biotechnol.* **33**, 495–502 (2015).
11. Farrell, J. A. *et al.* Single-cell reconstruction of developmental trajectories during zebrafish embryogenesis. *Science* **360**, eaar3131 (2018).
12. Wagner, D. E. *et al.* Single-cell mapping of gene expression landscapes and lineage in the zebrafish embryo. *Science* **360**, 981–987 (2018).
13. Farnsworth, D. R., Saunders, L. M. & Miller, A. C. A single-cell transcriptome atlas for zebrafish development. *Dev. Biol.* **459**, 100–108 (2020).
14. Raj, B. *et al.* Emergence of Neuronal Diversity during Vertebrate Brain Development. *Neuron* **108**, 1058-1074.e6 (2020).
15. Bradford, Y. M. *et al.* Zebrafish information network, the knowledgebase for *Danio rerio* research. *Genetics* **220**, iyac016 (2022).
16. Lange, M. *et al.* A multimodal zebrafish developmental atlas reveals the state-transition dynamics of late-vertebrate pluripotent axial progenitors. *Cell* **187**, 6742-6759.e17 (2024).

17. Gross-Thebing, T., Paksa, A. & Raz, E. Simultaneous high-resolution detection of multiple transcripts combined with localization of proteins in whole-mount embryos. *BMC Biol.* **12**, 55 (2014).
18. Westerfield, M. *The Zebrafish Book*. (University of Oregon Press, 2007).
19. Tuttle, A., Drerup, C. M., Marra, M., McGraw, H. & Nechiporuk, A. V. Retrograde Ret signaling controls sensory pioneer axon outgrowth. *eLife* **8**, e46092 (2019).
20. Jukic, A. *et al.* Presynaptic Nrxn3 is essential for ribbon-synapse maturation in hair cells. *Development* **151**, dev202723 (2024).
21. Lukasz, D. & Kindt, K. S. In Vivo Calcium Imaging of Lateral-line Hair Cells in Larval Zebrafish. *J. Vis. Exp.* 58794 (2018) doi:10.3791/58794.
22. Barbacid, M. Structural and Functional Properties of the TRK Family of Neurotrophin Receptors. *Ann. N. Y. Acad. Sci.* **766**, 442–458 (1995).
23. Riccio, A., Pierchala, B. A., Ciarallo, C. L. & Ginty, D. D. An NGF-TrkA-Mediated Retrograde Signal to Transcription Factor CREB in Sympathetic Neurons. *Science* **277**, 1097–1100 (1997).
24. Watson, F. L. *et al.* Rapid nuclear responses to target-derived neurotrophins require retrograde transport of ligand-receptor complex. *J. Neurosci. Off. J. Soc. Neurosci.* **19**, 7889–7900 (1999).
25. Ye, H., Kuruvilla, R., Zweifel, L. S. & Ginty, D. D. Evidence in support of signaling endosome-based retrograde survival of sympathetic neurons. *Neuron* **39**, 57–68 (2003).
26. Wickramasinghe, S. R. *et al.* Serum response factor mediates NGF-dependent target innervation by embryonic DRG sensory neurons. *Neuron* **58**, 532–545 (2008).
27. Zhou, B., Cai, Q., Xie, Y. & Sheng, Z.-H. Snapin recruits dynein to BDNF-TrkB signaling endosomes for retrograde axonal transport and is essential for dendrite growth of cortical neurons. *Cell Rep.* **2**, 42–51 (2012).
28. Vega, Q. C., Worby, C. A., Lechner, M. S., Dixon, J. E. & Dressler, G. R. Glial cell line-derived neurotrophic factor activates the receptor tyrosine kinase RET and promotes kidney morphogenesis. *Proc. Natl. Acad. Sci.* **93**, 10657–10661 (1996).
29. Kawai, K. & Takahashi, M. Intracellular RET signaling pathways activated by GDNF. *Cell Tissue Res.* **382**, 113–123 (2020).
30. Tsui, C. C. & Pierchala, B. A. The Differential Axonal Degradation of Ret Accounts for Cell-Type-Specific Function of Glial Cell Line-Derived Neurotrophic Factor as a Retrograde Survival Factor. *J. Neurosci.* **30**, 5149–5158 (2010).

31. Baker, P. A., Ibarra-García-Padilla, R., Venkatesh, A., Singleton, E. W. & Uribe, Rosa. A. *In toto* imaging of early enteric nervous system development reveals that gut colonization is tied to proliferation downstream of Ret. *Development* **149**, dev200668 (2022).
32. Trupp, M. *et al.* Peripheral expression and biological activities of GDNF, a new neurotrophic factor for avian and mammalian peripheral neurons. *J. Cell Biol.* **130**, 137–148 (1995).
33. Molliver, D. C. *et al.* IB4-Binding DRG Neurons Switch from NGF to GDNF Dependence in Early Postnatal Life. *Neuron* **19**, 849–861 (1997).
34. Oppenheim, R. W. *et al.* Glial Cell Line-Derived Neurotrophic Factor and Developing Mammalian Motoneurons: Regulation of Programmed Cell Death Among Motoneuron Subtypes. *J. Neurosci.* **20**, 5001–5011 (2000).
35. Whitehead, J., Keller-Peck, C., Kucera, J. & Tourtellotte, W. G. Glial cell-line derived neurotrophic factor-dependent fusimotor neuron survival during development. *Mech. Dev.* **122**, 27–41 (2005).
36. Kramer, E. R. *et al.* Cooperation between GDNF/Ret and ephrinA/EphA4 Signals for Motor-Axon Pathway Selection in the Limb. *Neuron* **50**, 35–47 (2006).
37. Luo, W. *et al.* A Hierarchical NGF Signaling Cascade Controls Ret-Dependent and Ret-Independent Events during Development of Nonpeptidergic DRG Neurons. *Neuron* **54**, 739–754 (2007).
38. Luo, W., Enomoto, H., Rice, F. L., Milbrandt, J. & Ginty, D. D. Molecular Identification of Rapidly Adapting Mechanoreceptors and Their Developmental Dependence on Ret Signaling. *Neuron* **64**, 841–856 (2009).
39. Haase, G. *et al.* GDNF Acts through PEA3 to Regulate Cell Body Positioning and Muscle Innervation of Specific Motor Neuron Pools. *Neuron* **35**, 893–905 (2002).
40. Vrieseling, E. & Arber, S. Target-Induced Transcriptional Control of Dendritic Patterning and Connectivity in Motor Neurons by the ETS Gene Pea3. *Cell* **127**, 1439–1452 (2006).
41. Luo, W. *et al.* A Hierarchical NGF Signaling Cascade Controls Ret-Dependent and Ret-Independent Events during Development of Nonpeptidergic DRG Neurons. *Neuron* **54**, 739–754 (2007).
42. Meltzer, S., Santiago, C., Sharma, N. & Ginty, D. D. The cellular and molecular basis of somatosensory neuron development. *Neuron* **109**, 3736–3757 (2021).
43. Sharma, N. *et al.* The emergence of transcriptional identity in somatosensory neurons. *Nature* **577**, 392–398 (2020).
44. Thomas, E. D., Cruz, I. A., Hailey, D. W. & Raible, D. W. There and back again: development and regeneration of the zebrafish lateral line system. *WIREs Dev. Biol.* **4**, 1–16 (2015).

45. Valera, G. *et al.* A neuronal blueprint for directional mechanosensation in larval zebrafish. *Curr. Biol.* **31**, 1463-1475.e6 (2021).
46. Schlosser, G. Induction and specification of cranial placodes. *Dev. Biol.* **294**, 303–351 (2006).
47. Breau, M. A. & Schneider-Maunoury, S. Cranial placodes: Models for exploring the multi-facets of cell adhesion in epithelial rearrangement, collective migration and neuronal movements. *Dev. Biol.* **401**, 25–36 (2015).
48. Schuster, K., Dambly-Chaudière, C. & Ghysen, A. Glial cell line-derived neurotrophic factor defines the path of developing and regenerating axons in the lateral line system of zebrafish. *Proc. Natl. Acad. Sci.* **107**, 19531–19536 (2010).
49. Thisse, C. & Thisse, B. High Throughput Expression Analysis of ZF-Models Consortium Clones. *ZFIN Direct Data Submiss.* http://zfin.org (2005).
50. Gasanov, E. V., Rafieva, L. M. & Korzh, V. P. BDNF-TrkB Axis Regulates Migration of the Lateral Line Primordium and Modulates the Maintenance of Mechanoreceptor Progenitors. *PLOS ONE* **10**, e0119711 (2015).
51. Nittoli, V. *et al.* A comprehensive analysis of neurotrophins and neurotrophin tyrosine kinase receptors expression during development of zebrafish. *J. Comp. Neurol.* **526**, 1057–1072 (2018).
52. Liao, J. C. & Haehnel, M. Physiology of afferent neurons in larval zebrafish provides a functional framework for lateral line somatotopy. *J. Neurophysiol.* **107**, 2615–2623 (2012).
53. Gompel, N., Dambly-Chaudière, C. & Ghysen, A. Neuronal differences prefigure somatotopy in the zebrafish lateral line. *Development* **128**, 387–393 (2001).
54. Matsuda, H. & Kubota, Y. Zebrafish pancreatic β cell clusters undergo stepwise regeneration using Neurod1-expressing cells from different cell lineages. *Cell Tissue Res.* **394**, 131–144 (2023).
55. Wilson, A. L. *et al.* Cadherin-4 plays a role in the development of zebrafish cranial ganglia and lateral line system. *Dev. Dyn. Off. Publ. Am. Assoc. Anat.* **236**, 893–902 (2007).
56. Andermann, P., Ungos, J. & Raible, D. W. Neurogenin1 defines zebrafish cranial sensory ganglia precursors. *Dev. Biol.* **251**, 45–58 (2002).
57. Gilmour, D., Knaut, H., Maischein, H.-M. & Nüsslein-Volhard, C. Towing of sensory axons by their migrating target cells in vivo. *Nat. Neurosci.* **7**, 491–492 (2004).
58. Pujol-Martí, J., Baudoin, J., Faucherre, A., Kawakami, K. & López-Schier, H. Progressive neurogenesis defines lateralis somatotopy. *Dev. Dyn.* **239**, 1919–1930 (2010).
59. Sato, A., Koshida, S. & Takeda, H. Single-cell analysis of somatotopic map formation in the zebrafish lateral line system. *Dev. Dyn.* **239**, 2058–2065 (2010).

60. Liao, J. C. & Haehnel, M. Physiology of afferent neurons in larval zebrafish provides a functional framework for lateral line somatotopy. *J. Neurophysiol.* **107**, 2615–2623 (2012).
61. Jiang, T., Kindt, K. & Wu, D. K. Transcription factor Emx2 controls stereociliary bundle orientation of sensory hair cells. *eLife* **6**, e23661 (2017).
62. Sommer, B., Köhler, M., Sprengel, R. & Seeburg, P. H. RNA editing in brain controls a determinant of ion flow in glutamate-gated channels. *Cell* **67**, 11–19 (1991).
63. Brusa, R. *et al.* Early-Onset Epilepsy and Postnatal Lethality Associated with an Editing-Deficient *GluR-B* Allele in Mice. *Science* **270**, 1677–1680 (1995).
64. Higuchi, M. *et al.* Point mutation in an AMPA receptor gene rescues lethality in mice deficient in the RNA-editing enzyme ADAR2. *Nature* **406**, 78–81 (2000).